Atomistic simulations of complex materials: ground-state and excited-state properties

2002 J. Phys.: Condens. Matter 14 3015

(http://iopscience.iop.org/0953-8984/14/11/313)

INSTITUTE OF PHYSICS PUBLISHING JOURNAL OF PHYSICS: CONDENSED MATTER

J. Phys.: Condens. Matter **14** (2002) 3015–3047 PII: S0953-8984(02)29842-2

Atomistic simulations of complex materials: ground-state and excited-state properties

Thomas Frauenheim[1], **Gotthard Seifert**[1], **Marcus Elstner**[1,2], **Thomas Niehaus**[1,2], **Christof Köhler**[1,2], **Marc Amkreutz**[1], **Michael Sternberg**[1], **Zoltán Hajnal**[1], **Aldo Di Carlo**[3] **and Sándor Suhai**[2]

[1] Universität Paderborn, Fachbereich Physik, Theoretische Physik, 33095 Paderborn, Germany
[2] Deutsches Krebsforschungszentrum, Abteilung Molekulare Biophysik, Im Neuenheimer Feld 280, 66192 Heidelberg, Germany
[3] Universita di Roma 'Tor Vergata', Dipartimento di Ingegneria Elettronica, Via di Tor Vergata n. 110, 00133 Roma, Italy

Received 18 October 2001, in final form 8 January 2002
Published 8 March 2002
Online at stacks.iop.org/JPhysCM/14/3015

Abstract

The present status of development of the density-functional-based tight-binding (DFTB) method is reviewed. As a two-centre approach to density-functional theory (DFT), it combines computational efficiency with reliability and transferability. Utilizing a minimal-basis representation of Kohn–Sham eigenstates and a superposition of optimized neutral-atom potentials and related charge densities for constructing the effective many-atom potential, all integrals are calculated within DFT. Self-consistency is included at the level of Mulliken charges rather than by self-consistently iterating electronic spin densities and effective potentials. Excited-state properties are accessible within the linear response approach to time-dependent (TD) DFT. The coupling of electronic and ionic degrees of freedom further allows us to follow the non-adiabatic structure evolution via coupled electron–ion molecular dynamics in energetic particle collisions and in the presence of ultrashort intense laser pulses. We either briefly outline or give references describing examples of applications to ground-state and excited-state properties. Addressing the scaling problems in size and time generally and for biomolecular systems in particular, we describe the implementation of the parallel 'divide-and-conquer' order-N method with DFTB and the coupling of the DFTB approach as a quantum method with molecular mechanics force fields.

1. Introduction

Considerable advances in the theoretical framework for studying the structure and properties of materials have been achieved. Coupled with the advent of ever more powerful computers, this has enabled the development of new algorithms for the computational modelling of materials.

As the field of computational materials science develops and matures, the notion is becoming established in the community that modelling efforts are an integral part of interdisciplinary materials research.

Nowadays, besides common inorganic crystalline and amorphous solids (bulk, defects, surfaces, adsorbates, interfaces), a broad variety of clusters, cluster-assembled matter, fullerenes, nanotubes, organic molecular, polymeric, and biomolecular structures are also considered. As the main goal, computational materials science is aiming to improve the atomic-scale understanding of materials structures and properties. Structure–property correlations, that are never resolved in experiments on a molecular level, are thus becoming quantified. In this context, atomistic simulations begin to contribute to the optimization of materials properties by allowing tailoring of structures and chemical compositions for a broad range of applications.

At present, many advanced technological developments in nanoscale electronics, optoelectronics, and photonics are based upon complex functionalization of inorganic substrates with either self-assembled organic layers or biomolecular structures. A challenging task in computational modelling is pushing the limits and addressing biomolecular systems in their natural environment in order to study their function, e.g. the visual cascade in rhodopsin or the photosynthetic activity in bacteriorhodopsin. The fundamental understanding of underlying mechanisms will provide essential knowledge for improving on Nature and designing new concepts for future technologies in molecular electronics, optical data, and energy storage.

In considering the growing complexity in materials research with the claim of broad technological relevance, robust simulation methods have to combine transferability with high computational efficiency. In turn, the sophistication of methods for determining complex potential energy hypersurfaces of many-atom arrangements will crucially dictate the quality of the simulated structures and the validity of physical and chemical data that can be used to permit 'handshaking' with experiments. On the other hand, the complexity of the potential energy surface determines the amount of computer time required. This will become particularly important in the study of materials dynamics during growth processes and in coupling to strong laser fields.

Today, empirically derived potentials [1–5] dominate in large-scale materials simulations addressing problems of technological relevance. However, since they are adapted to a finite set of equilibrium situations (mostly experimental data and *ab initio* results for equilibrium configurations), they usually apply well to systems that are within the parametrization space, but usually fail far from those. Additionally, they are not transferable to different chemical situations and more generally to calculations of spectroscopic data relying quantitatively on the detailed knowledge of the electronic structure.

In conclusion, for large-scale applications, a method based on quantum mechanics is highly desirable. It should allow one to follow with confidence the structural dynamics during the time evolution in chemical reactions and bond formation. The equilibrium configurations have to be accurately described as regards details of the geometry, and cohesive and elastic properties, including stability as well as vibrational dynamics. The method has to perform equally well for very different types of material and inherently should yield electronic structure information to enable comparison of theoretical with spectroscopic data. Furthermore, the predictive quantum mechanical treatment of the complex many-atom structures, taking advantage of reliable approximations, should be implemented efficiently for running on advanced computer architectures. In this regard the number of atoms that at maximum might be included in one system, the number of structures that are obtained for scanning configuration space, and the time for which one can follow the structural evolution during pattern formation are key factors. These are becoming even more crucial in cases where dynamic structure simulations

involving energetic particle collisions or the presence of strong laser fields are considered. Additionally, in order to meet the requirements for considering structure formation in organic and biomolecular systems, in solution or e.g. in a natural protein environment, besides strongly covalent and ionic bonding interactions, the weak chemical interactions of hydrogen bonding and van der Waals type also need to be taken into account at an appropriate level.

Focusing now on electronic structure methods in materials simulations, the highest accuracy is achieved by sophisticated '*ab initio*' methods. These are post-Hartree–Fock [6] and quantum Monte Carlo [7] methods which rely on a proper evaluation of many-particle wavefunctions and the explicit inclusion of electronic exchange and correlation interactions. However, due to their high computational demand, their scaling behaviour with increasing particle number which is $\propto N^{(4-5)}$ makes them hardly applicable to larger systems and complex solids. By strongly reducing the configuration space for the setting up of wavefunctions, today's largest systems in such calculations reach a few dozen atoms. Consequently, in any applications, model-like situations rather than technologically relevant ones are considered.

Considering larger molecular clusters or nanostructures and periodic solids in supercells with 100–200 atoms, density-functional theory (DFT) [8,9] in the local density approximation and with gradient corrections (LDA/GGA) for the exchange–correlation functional has proven to be the method of choice in numerous successful applications for very different problems and material types. In replacing the complex many-electron wavefunction by the electron density, DFT transforms the solution of the electronic structure for a many-atom system into an effective one-particle problem. Using common approximations for the exchange–correlation functional, the self-consistent solution of the Kohn–Sham equation determines the effective potential at which the electrons establish their ground-state density, simultaneously minimizing the total energy of the system. High accuracy in such calculations will only be established if the basis for representing the single-particle electron states has converged. Making use of efficient molecular dynamics (MD) within plane-wave basis sets [10], unconstrained simulated annealing studies are currently following structure formation, e.g. of amorphous semiconductors in periodically arranged supercells of about 100 atoms over 1–2 ps [11]. These simulations usually generate single configurations with an extent, in terms of structural evolution of the system in the ground state, that is orders of magnitude short of real processing timescales.

To account also for excited-state dynamics and properties, DFT has been generalized to incorporate TD external fields [12]. A quantum–classical Lagrangian ansatz for describing the coupled electron–ion dynamics [13] here opens the way to performing non-adiabatic MD simulations of structure formation, e.g. involving energetic collisions of particles and clusters, or to studying the behaviour of complex materials interacting with strong laser fields. Since under these circumstances the electron rather than the dynamics of the nuclei determines the timescale for integration, the system sizes and time extent for simulations are even more restricted.

For the foreseeable future the computational demands for describing structural, electronic, and dynamical properties of large and complex materials with technologically relevant size, simulation time, and statistics demand approximate solutions.

In this context, empirical tight-binding (TB) methods have been developed and used in solid-state physics. Due to their conceptional simplicity, in most cases even neglecting self-consistency, they more easily address the size problems; for a review, see e.g. [14]. There have been numerous successful applications to a broad range of materials and systems [15–18]. Additional developments take advantage of the strongly localized character of electronic interactions in the model (usually restricted to nearest neighbours only) and, together with so-called order-N methods [19–21], provide techniques for simulating structures with several

hundred or even thousand atoms over a short time. Although the TB approach is based on quantum mechanics, it lacks reliability and transferability due to the parametrization of the electronic Hamiltonian with respect to a finite set of equilibrium structures and properties. Additionally, there is serious weakness in having no well-defined procedure for constructing the required data from an atomic basis (wavefunctions and potentials) in a way which could include any desired chemical element.

Therefore, during the last decade we have put a strong effort into the development of approximate methods, which try to merge the spirit and reliability of DFT with the simplicity and efficiency of TB ansatze. In keeping the computational cost but simultaneously also the number of parameters as small as possible, the method described here and related computer codes offer a high degree of transferability as well as universality for both ground-state and excited-state properties. Thus we claim that the method operates at the same accuracy and efficiency whether organic molecules or solids, clusters, insulators, semi-conductors and metals or even biomolecular systems are investigated, and, furthermore, independent of the type of atoms which constitute the material.

In the present article we will briefly outline the DFT foundation of the method, which is introduced as the density-functional-based tight-binding (DFTB) approach in section 2. In section 2.1, we describe a variational treatment of an approximate Kohn–Sham energy functional given by a second-order perturbation expansion with respect to charge-density fluctuations around a properly chosen reference density. In further applying well-balanced simplifications, the variational minimization of the energy functional yields a modified Kohn–Sham-like equation for determining the ground-state properties of many-atom structures, in which the self-consistency in the effective potential and the charge density is replaced by a much simpler self-consistency in the distribution of Mulliken charges. The method includes special optimization of accuracy with respect to the use of a minimal basis set for representing the single-electron Kohn–Sham-like eigenstates. The procedure described allows one to predetermine the electronic interactions within a two-centre picture using an effective Hamiltonian given at a properly chosen reference density. Inter-atomic forces for adiabatic MD simulations are easily calculated analytically, which favours efficient total-energy minimization of many-atom structures, such as nanostructured bulk, surface, or molecular cluster systems in their ground state. While section 2.1 is focused entirely on ground-state properties, a TD generalization of DFTB within a linear response formulation of TDDFT is described in section 2.2. The approach described allows one to account efficiently for excited-state properties and related optical spectra in molecular systems. However, to describe processes such as those in ultrashort-time laser spectroscopy, the correct description of the excitation process and following the structural dynamics in the excited state requires a non-perturbative treatment of the radiation fields combined with a direct numerical propagation of the TD electronic wavefunctions. This problem will be addressed in section 2.3 where we describe a general TD quantum mechanical treatment of laser-induced non-adiabatic structural dynamics on coupled ground-state and excited-state potential energy surfaces. Finally, in section 2.4 details of the computational realization of the method, the construction of the optimized reference density within the minimal-basis description, and the introduction of the integral approximations used are given.

Further, in order to meet the demands for simulations of organic and biomolecular systems, we describe in section 3 as an additional development the incorporation of weak van der Waals (vdW) forces using a London dispersion formula and the implementation of the divide-and-conquer (DAC) linear scaling method for an efficient calculation of the electronic total energy of large systems. In finally addressing the embedding of the quantum mechanically treated

structures into a natural environment, we outline the coupling of the DFTB approach as a quantum mechanical (QM) method to molecular mechanics (MM) via a QM/MM interface.

We further discuss in section 4 how theoretical data may provide 'handshaking' with experimental measurements. This will include vibrational and optical spectra (IR), pump–probe ultrashort-time laser spectroscopy, electron spin as well as nuclear magnetic resonance data (EPR/NMR), scanning probe imaging (STM), electrical conductivity, and current–voltage spectroscopy in molecular and semiconductor heterojunctions.

2. Method

2.1. Basic concepts of the density-functional-based tight-binding method

The Kohn–Sham total-energy expression of DFT in atomic units with the electron density $n = n_\uparrow(\boldsymbol{r}) + n_\downarrow(\boldsymbol{r})$ and the magnetization density $\mu(\boldsymbol{r}) = n_\uparrow(\boldsymbol{r}) - n_\downarrow(\boldsymbol{r})$,

$$E_{\mathrm{tot}}^{\mathrm{DFT}} = \sum_{\sigma=\uparrow,\downarrow} \sum_{i}^{\mathrm{occ}} n_{i\sigma} \left\{ \langle \psi_{i\sigma} | -\frac{\nabla^2}{2} + v + \frac{1}{2} \int \frac{n(\boldsymbol{r}')\, \mathrm{d}^3 r'}{|\boldsymbol{r} - \boldsymbol{r}'|} | \psi_{i\sigma} \rangle \right\} + E_{\mathrm{xc}}[n, \mu] + \underbrace{\frac{1}{2} \sum_{\alpha\beta}^{N} \frac{Z_\alpha Z_\beta}{|\boldsymbol{R}_\alpha - \boldsymbol{R}_\beta|}}_{E_{\alpha\beta}}, \tag{1}$$

is transformed by decomposing the electron density into a sum of a reference density and a density fluctuation, $n = n_0 + \delta n$. For brevity, $n_0(\boldsymbol{r})$, $n(\boldsymbol{r})$, $\mu(\boldsymbol{r})$ and $n_0(\boldsymbol{r}')$, $n(\boldsymbol{r}')$, $\mu(\boldsymbol{r}')$ have been replaced by n_0, n, μ and n_0', n', μ', respectively. N is the number of atoms in the system and v is the external potential.

By further expanding $E_{\mathrm{xc}}[n, \mu]$ around the reference densities $n = n_0$ and $\mu = 0$ up to second order in the density fluctuations, we obtain [22, 23]

$$\begin{aligned} E_{\mathrm{tot}} = {} & \sum_{\sigma=\uparrow,\downarrow} \sum_{i}^{\mathrm{occ}} n_{i\sigma} \langle \psi_{i\sigma} | \underbrace{-\frac{\nabla^2}{2} + v + \int \frac{n_0'\, \mathrm{d}^3 r'}{|\boldsymbol{r} - \boldsymbol{r}'|} + V_{\mathrm{xc}}[n_0, 0]}_{\hat{H}^0[n_0]} | \psi_{i\sigma} \rangle \\ & + \frac{1}{2} \int\int \left(\frac{1}{|\boldsymbol{r} - \boldsymbol{r}'|} + \frac{\delta^2 E_{\mathrm{xc}}}{\delta n\, \delta n'} |_{n_0,0} \right) \delta n\, \delta n'\, \mathrm{d}^3 r\, \mathrm{d}^3 r' \\ & + \frac{1}{2} \int\int \frac{\delta^2 E_{\mathrm{xc}}}{\delta \mu\, \delta \mu'} |_{n_0,0} \delta\mu\, \delta\mu'\, \mathrm{d}^3 r\, \mathrm{d}^3 r' + E_{\alpha\beta} + E_{\mathrm{xc}}[n_0, 0] \\ & - \int V_{\mathrm{xc}}[n_0, 0] n_0\, \mathrm{d}^3 r - \frac{1}{2} \int\int \frac{n_0 n_0'}{|\boldsymbol{r} - \boldsymbol{r}'|}\, \mathrm{d}^3 r\, \mathrm{d}^3 r'. \end{aligned} \tag{2}$$

To derive the total energy within the DFTB approximation, the energy contributions in equation (2) are further subjected to the following approximations:

(a) The Hamiltonian matrix elements $\langle \psi_{i\sigma} | \hat{H}^0 | \psi_{i\sigma} \rangle$ are represented in a minimal basis of optimized pseudo-atomic orbitals φ_μ; see section 2.4.1:

$$\psi_{i\sigma} = \sum_\mu c_{\mu i\sigma} \varphi_\mu(\boldsymbol{r} - \boldsymbol{R}_\alpha). \tag{3}$$

As Hamiltonian matrix elements $H_{\mu\nu}^0$ in this basis, we take the atomic eigenvalues of free spin-unpolarized atoms to account for the diagonal elements $H_{\mu\mu}^0$ and calculate the non-diagonal elements $H_{\mu\nu}^0$ within the two-centre approximation [23–25]:

$$H_{\mu\nu}^0 = \langle \varphi_\mu | \hat{T} + V_{\mathrm{eff}}[n_\alpha^0 + n_\beta^0] | \varphi_\nu \rangle \qquad \mu \in \alpha,\ \nu \in \beta. \tag{4}$$

The $H^0_{\mu\nu}$ are tabulated together with the overlap matrix elements $S_{\mu\nu}$ with respect to the interatomic distance $R_{\alpha\beta}$. V_{eff} is the effective Kohn–Sham potential superposing the ionic, Hartree and exchange–correlation contributions, where the $n^0_{\alpha,\beta}$ are the densities of the neutral pseudo-atoms α and β; $\hat{T}$ is the kinetic energy operator.

(b) The charge-density fluctuations δn in the second term of equation (2) are written as a superposition of atomic contributions δn_α:

$$\delta n = \sum_\alpha \delta n_\alpha, \tag{5}$$

which are approximated by monopolar charge fluctuations at the atoms α, $\Delta q_\alpha = q_\alpha - q^0_\alpha$. q^0_α is the number of electrons of the neutral atom α and the q_α are determined from a Mulliken population analysis. The second-order term in δn of the energy, equation (2), can then be approximated by

$$\frac{1}{2}\int\int\left(\frac{1}{|\boldsymbol{r}-\boldsymbol{r}'|}+\left.\frac{\delta^2 E_{\text{xc}}}{\delta n\,\delta n'}\right|_{n_0,0}\right)\delta n\;\delta n'\,\mathrm{d}^3r\,\mathrm{d}^3r' \approx \sum_{\alpha\beta}\gamma_{\alpha\beta}(|\boldsymbol{R}_\alpha-\boldsymbol{R}_\beta|)\,\Delta q_\alpha\,\Delta q_\beta. \tag{6}$$

For $\alpha \neq \beta$, $\gamma_{\alpha\beta}$ is determined analytically from the Coulomb interaction of two atom-centred spherical charge distributions [22] located at $\boldsymbol{R}_\alpha$ and $\boldsymbol{R}_\beta$. The on-site contributions $\gamma_{\alpha\alpha}$ are determined by spin-unpolarized atomic DFT calculations as second derivatives of the total atom energy with respect to the charge and the occupation number, respectively; see section 2.4.2.

The terms discussed so far together with the double counting and ion–ion repulsion contributions in the last line of equation (2) cover all electronic contributions which depend on the reference density n_0 and the density fluctuation δn. Neglecting at this stage the fluctuations of the magnetization density $\delta\mu$, this allows for a spin-unpolarized self-consistent treatment of charge-transfer effects. This level of approximation, introduced as the self-consistent-charge DFTB (SCC-DFTB) approximation in [22], has been successfully applied to a large variety of problems, including organic molecules, semiconductor structures and biomolecular systems [23, 26, 27].

(c) The third term in equation (2) is the only one that directly depends on the fluctuation of the magnetization density. By expanding the magnetization density in non-overlapping spherically symmetric functions $f_{\alpha l}(|\boldsymbol{r}-\boldsymbol{R}_\alpha|)$ centred on atom α and depending on the angular momentum l:

$$\mu(\boldsymbol{r}) = \sum_\alpha^N \sum_{l\in\alpha} p_{\alpha l}\, f_{\alpha l}(|\boldsymbol{r}-\boldsymbol{R}_\alpha|), \tag{7}$$

this term can be transformed for local and semi-local density functionals into the expression

$$\begin{aligned}\frac{1}{2}\int\left.\frac{\delta^2 E_{\text{xc}}}{\delta\mu^2}\right|_{n_0,0}\delta\mu^2\,\mathrm{d}^3r &\approx \frac{1}{2}\sum_\alpha^N\sum_{l\in\alpha}\sum_{l'\in\alpha} p_{\alpha l}\,p_{\alpha l'}\int f_{\alpha l}\left.\frac{\delta^2 E_{\text{xc}}}{\delta\mu^2}\right|_{n_0,0} f_{\alpha l'}\,\mathrm{d}^3r \\ &\approx \frac{1}{2}\sum_\alpha^N\sum_{l\in\alpha}\sum_{l'\in\alpha} p_{\alpha l}\,p_{\alpha l'}\,W_{\alpha l l'}.\end{aligned} \tag{8}$$

After substituting in equation (7) for the magnetization density, the integration only involves atomic quantities. Therefore, the integral in equation (8) can be approximated by a constant $W_{\alpha l l'}$ which is specific for every atom type; see section 2.4.3. The $W_{\alpha l l'}$ are resolved with respect to the angular momentum. This couples different angular momentum shells and is important, e.g., for the calculation of hyperfine-coupling constants; see section 4.4. The parameters $p_{\alpha l}$

in the series expansion are identified with the spin populations of the orbitals of each atom which can be obtained from the Mulliken populations in the different spin states:

$$p_{\alpha l} = q_{\alpha l\uparrow} - q_{\alpha l\downarrow}; \qquad q_{\alpha l\sigma} = \frac{1}{2}\sum_{i}^{\mathrm{occ}} n_{i\sigma} \sum_{\mu\in l\alpha}\sum_{\nu}^{N}(c^{*}_{\mu i\sigma}c_{\nu i\sigma}S_{\mu\nu} + c^{*}_{\nu i\sigma}c_{\mu i\sigma}S_{\nu\mu}). \tag{9}$$

(d) Finally, the remaining 'double-counting terms' (see equation (2)) and the ion–ion repulsion ($E_{\alpha\beta}$) are summarized into a short-range repulsive energy $E_{\mathrm{rep}} = \sum_{\alpha\neq\beta} U[R_{\alpha\beta}]$, consisting of atom-type specific pair potentials $U[R_{\alpha\beta}]$. These are constructed as the difference between the total energy versus distance calculated in DFT and the corresponding electronic energy derived within the DFTB approach for properly chosen reference systems. For a detailed discussion, see [23].

The total-energy expression in spin-polarized the DFTB (SDFTB) approach then takes the form

$$E^{\mathrm{SDFTB}}_{\mathrm{tot}} = \sum_{\sigma=\uparrow,\downarrow}\sum_{i}^{\mathrm{occ}} n_{i\sigma}\langle\psi_{i\sigma}|\hat{H}^{0}[n_0]|\psi_{i\sigma}\rangle + \frac{1}{2}\sum_{\alpha\beta}^{N}\gamma_{\alpha\beta}\,\Delta q_\alpha\,\Delta q_\beta + \frac{1}{2}\sum_{\alpha}^{N}\sum_{l\in\alpha}\sum_{l'\in\alpha} p_{\alpha l}\,p_{\alpha l'}W_{\alpha ll'} + E_{\mathrm{rep}}. \tag{10}$$

Note that only the third term contains the spin dependencies. Variation of this approximate Kohn–Sham energy expression with respect to the minimal basis yields single-particle 'Kohn–Sham-like' equations:

$$\sum_{\nu} c_{\nu i\sigma}(H_{\mu\nu\sigma} - \varepsilon_{i\sigma}S_{\mu\nu}) = 0 \qquad \forall\mu, i, \sigma, \tag{11}$$

where the Hamiltonian matrix elements are given by

$$H_{\mu\nu\sigma} = H^{0}_{\mu\nu} + \underbrace{\frac{1}{2}S_{\mu\nu}\sum_{\zeta}^{N}(\gamma_{\alpha\zeta} + \gamma_{\beta\zeta})\,\Delta q_\zeta}_{H^{1}_{\mu\nu}} \pm \frac{1}{2}S_{\mu\nu}\sum_{l''\in\alpha}(W_{\alpha ll''} + W_{\alpha l'l''})\,p_{\alpha l''}. \tag{12}$$

The plus and minus signs correspond to the Hamiltonian for spin-up and spin-down electrons, respectively. In our approximate theory, thus, the self-consistency with respect to the spin densities in DFT has been replaced by a self-consistency in the spin populations. While net charge fluctuations in $H^{1}_{\mu\nu}$ upon self-consistent iteration are correcting both on-site and off-site matrix elements, the spin-dependent corrections affect on-site matrix elements only.

Analytical interatomic forces easily can be calculated by differentiating the total energy with respect to the nuclear coordinates:

$$\boldsymbol{F}_{\alpha\sigma} = -\sum_{i} n_{i\sigma}\sum_{\mu}\sum_{\nu} c^{*}_{\mu i\sigma}c_{\nu i\sigma}\left(\frac{\partial H^{0}_{\mu\nu}}{\partial\boldsymbol{R}_\alpha} - \left(\varepsilon_{i\sigma} - \frac{H^{1}_{\mu\nu}}{S_{\mu\nu}} \pm \sum_{\tau} W_{\tau\mu}p_\tau\right)\frac{\partial S_{\mu\nu}}{\partial\boldsymbol{R}_\alpha}\right) - \Delta q_\alpha\sum_{\zeta}\frac{\partial\gamma_{\alpha\zeta}}{\partial\boldsymbol{R}_\alpha}\,\Delta q_\zeta - \frac{\partial E_{\mathrm{rep}}}{\partial\boldsymbol{R}_\alpha}. \tag{13}$$

2.2. TB approach to time-dependent density-functional response theory (TDDFRT)

In order to describe also situations where electrons are excited due to applied time-dependent fields, the original DFT formulation of Hohenberg and Kohn with its variational character has to be extended. A rigorous foundation of what is called time-dependent DFT (TDDFT) was

given by Runge and Gross, but not until the 1980s [28] (see [29] for a review). Similarly to the ground-state formulation, Kohn–Sham equations can also be derived in TDDFT, if one assumes the existence of a non-interacting reference system which possesses the same (now time-dependent) density as the true interacting system at hand. These may be solved in different ways. For low fluences of the external field, perturbation theory is applicable and yields in principle exact (provided the correct XC functional is known) excitation energies and oscillator strengths, i.e. the optical spectrum. The numerical effort required in such calculations is much lower than that of competing electronic structure methods like the correlated wavefunction [30, 31] or quasi-particle [32] approaches. At the same time, even using standard ground-state XC functionals, high-accuracy results were obtained for a wide range of different system classes including solids [33, 34], clusters [35, 36] and molecules [37, 38].

In the above-mentioned perturbation theory approach [39,40], also called time-dependent density-functional response theory, first an ordinary SCF calculation has to be performed. This yields single-particle KS orbitals ψ_i and the corresponding KS energies ε_i. Note that we consider only closed-shell systems. As is well known, simple energy differences of virtual and occupied orbitals are a poor approximation to the true excitations of a system. Singlet energies are strongly underestimated while the opposite is true for triplet states. Within TDDFRT this failure is remedied via introduction of the so-called coupling matrix:

$$K_{ij\sigma,kl\tau} = \int\int \psi_i(\boldsymbol{r})\psi_j(\boldsymbol{r}')\left(\frac{1}{|\boldsymbol{r}-\boldsymbol{r}'|} + \frac{\delta^2 E_{\mathrm{xc}}}{\delta n_\sigma\, \delta n'_\tau}\right)\psi_k(\boldsymbol{r})\psi_l(\boldsymbol{r}')\,\mathrm{d}^3r\,\mathrm{d}^3r' \tag{14}$$

(σ, τ are spin indices), which gives the response of the SCF potential with respect to a change in the electronic density.

The true excitation energies (ω_I) are then found by solving the eigenvalue problem:

$$\sum_{ij\sigma}\left[\omega_{ij}^2\delta_{ik}\delta_{jl}\delta_{\sigma\tau} + 2\sqrt{\omega_{ij}}K_{ij\sigma,kl\tau}\sqrt{\omega_{kl}}\right]\mathcal{F}^I_{ij\sigma} = \omega_I^2\mathcal{F}^I_{kl\tau}, \tag{15}$$

where $\omega_{ij} = \varepsilon_j - \varepsilon_i$ (i, k are occupied KS orbitals whereas j, l are unoccupied ones). Inspecting equation (15), it is apparent that not only are individual single-particle excitations ω_{ij} corrected, but also the couplings between different transitions ($i \to j, k \to l$) are properly taken into account, which allows for the description of collective effects.

Since direct numerical evaluation of the coupling matrix would be computationally highly demanding, we recently introduced the so-called γ-approximation to the coupling matrix (equation (14)) [41]. Here the principal idea is to rewrite equation (14) in a way in which only the LCAO coefficients (equation (3)) and known two-centre matrix elements are needed.

To do so, we first decompose the density of transition between different orbitals $p^{ij}(\boldsymbol{r}) = \psi_i(\boldsymbol{r})\psi_j(\boldsymbol{r})$ into atom-centred contributions $p^{ij}(\boldsymbol{r}) = \sum_\alpha p^{ij}_\alpha(\boldsymbol{r})$. Analogously to the ideas presented in section 2.1, the p^{ij}_α are further subjected to a multipole expansion and a subsequent monopole approximation:

$$p^{ij}_\alpha(\boldsymbol{r}) \approx q^{ij}_\alpha F_\alpha(\boldsymbol{r}), \tag{16}$$

where q^{ij}_α are the Mulliken atomic transition charges:

$$q^{ij}_\alpha = \frac{1}{2}\sum_{\mu\in\alpha}\sum_\nu (c_{\mu i}c^*_{\nu j}S_{\mu\nu} + c_{\nu i}c^*_{\mu j}S_{\nu\mu}). \tag{17}$$

Like in section 2.1, it is useful to work in the set of variables $n = n_\uparrow + n_\downarrow$ (the total density) and $\mu = n_\uparrow - n_\downarrow$ (the magnetization). If the ground-state density is spin unpolarized, we have

$$\frac{\delta^2 E_{\mathrm{xc}}}{\delta n_\sigma\, \delta n'_\tau} = \frac{\delta^2 E_{\mathrm{xc}}}{\delta n\, \delta n'} + (2\delta_{\sigma\tau} - 1)\frac{\delta^2 E_{\mathrm{xc}}}{\delta\mu\, \delta\mu'}. \tag{18}$$

and the coupling matrix, equation (14), now takes the following form:

$$K_{ij\sigma,kl\tau} = \sum_{\alpha\beta} q_\alpha^{ij} q_\beta^{kl} (\tilde{\gamma}_{\alpha\beta} + (2\delta_{\sigma\tau} - 1)\mu_{\alpha\beta}), \tag{19}$$

where

$$\tilde{\gamma}_{\alpha\beta} = \int\int \left(\frac{1}{|\boldsymbol{r} - \boldsymbol{r}'|} + \frac{\delta^2 E_{\mathrm{xc}}}{\delta n\, \delta n'}|_{n,0} \right) F_\alpha(\boldsymbol{r}) F_\beta(\boldsymbol{r}')\, \mathrm{d}^3 r\, \mathrm{d}^3 r', \tag{20}$$

$$\mu_{\alpha\beta} = \int\int \left. \frac{\delta^2 E_{\mathrm{xc}}}{\delta\mu\, \delta\mu'} \right|_{n,0} F_\alpha(\boldsymbol{r}) F_\beta(\boldsymbol{r}')\, \mathrm{d}^3 r\, \mathrm{d}^3 r'. \tag{21}$$

Comparison of equations (20) and (6) shows that $\tilde{\gamma}_{\alpha\beta}$ and $\gamma_{\alpha\beta}$ only differ in the actual density entering the E_{xc}-derivative. This difference could in principle be taken into account, but test calculations show that for most covalently bound systems the influence of charge transfer can safely be neglected, leading to $\tilde{\gamma}_{\alpha\beta} = \gamma_{\alpha\beta}$. The same holds for the integral involving the magnetization, equation (21), which we approximate to be on-site in accordance with equation (8): $\mu_{\alpha\beta} = \delta_{\alpha\beta} W_\alpha$. Note that in contrast to the case for equation (8), here the magnetization parameter W_α is not resolved according to angular momentum.

With these approximations, the coupling matrix, equation (19), can be easily constructed. The excitation energies obtained from equation (15) and the required singlet oscillator strengths can be calculated using [39]

$$f^I = \frac{2}{3}\omega^I \sum_{k=x,y,z} \left| \sum_{ij} \langle \psi_i | r_k | \psi_j \rangle \sqrt{\frac{\omega_{ij}}{\omega^I}} (\mathcal{F}^I_{ij\uparrow} + \mathcal{F}^I_{ij\downarrow}) \right|^2, \tag{22}$$

where the transition dipole matrix elements are

$$\langle \psi_i | \boldsymbol{r} | \psi_j \rangle = \sum_\alpha \boldsymbol{R}_\alpha q_\alpha^{ij}. \tag{23}$$

The main features of the above-described γ-approximation may be summed up in the following way. First, it is a parameter-free approach, i.e. no experimentally derived quantities enter the scheme, leading to a high transferability. Second, it goes beyond the single-particle picture, covering situations where electron–hole interaction is an important issue. Third, it can in principle be used in conjunction with any TB scheme. Fourth, it is numerically efficient.

The last point stems from the fact that no explicit integral evaluations need to be performed during the run time of the program. Together with the employment of a minimal basis this leads to a substantial speeding up compared to full TDDFRT calculations as shown in figure 1. For very large systems, the bottleneck is the solution of the eigenvalue problem in equation (15). In these cases one should take advantage of the sparsity of the coupling matrix or use iterative techniques to further reduce the computational effort.

Of course, even the fastest method is of no use if it yields qualitatively wrong results. The performance of the γ-approximation has therefore been studied in detail in [41] and [43]. A short summary will be reported in section 4, presenting also some new results for sulphur–organic compounds.

2.3. Time-dependent generalization of the DFTB approach

In the last section we have shown that TDDFT can be used to calculate optical spectra in the regime of linear response. For high intensities of the applied fields, which are easily obtained from today's subpicosecond laser sources, however, this perturbation theory breaks down and one is left with the complicated task of solving the TD-KS equations exactly. This can be done numerically, but the time step of such a solution has to fall into the range of the electron

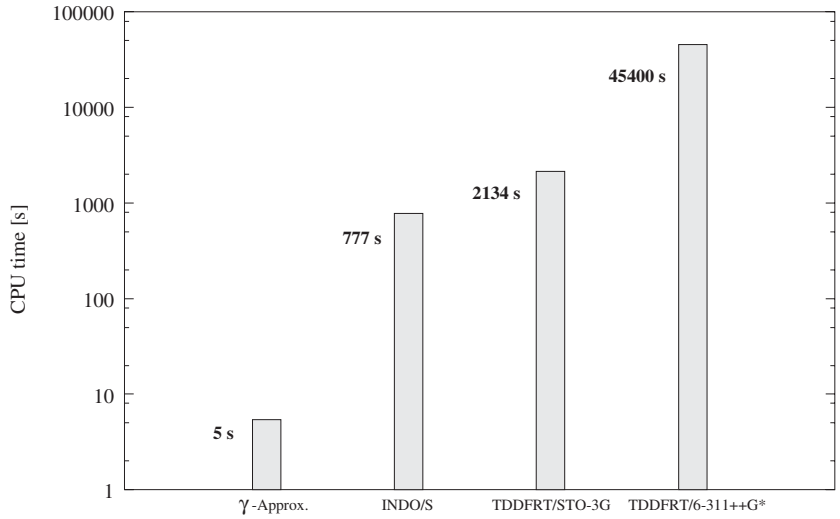

Figure 1. Comparison of CPU usage for different methods including the quantum chemical INDO/S [42] approach as well as TDDFRT with different basis sets. Shown is the total CPU time in seconds for the complete set of organic molecules from [41]. The calculations have been performed on a single node of the HP Exemplar V-Class system; for details see [41, 43].

dynamics timescale. This is in contrast to the case for standard quantum MD simulations where the timescale is set by the much slower nuclei. Consequently, first-principles approaches are limited to very short simulation times [44] or extremely small system sizes [45]. To overcome these limits, we show in this section how the typical DFTB approximations can also be used in a time-dependent framework.

For simulating the coupled motion of ions and electrons in the presence of strong laser fields, we use as starting point the following quantum–classical Lagrangian [43, 46]:

$$\mathcal{L} = \sum_{\alpha} \tfrac{1}{2} M_\alpha \dot{\boldsymbol{R}}_\alpha^2 - \sum_i n_i \langle \Psi_i(t) | H(t) - \mathrm{i}(\overleftrightarrow{\mathrm{d}/\mathrm{d}t}) | \Psi_i(t) \rangle - E_{\mathrm{DC}} - E_{\alpha\beta}, \quad (24)$$

where the symbol $\leftrightarrow$ stands for a symmetrized derivative, H represents the common DFT Hamiltonian, which may explicitly depend on time due to external fields, and the double-counting contributions E_{DC}:

$$E_{\mathrm{DC}} = -\frac{1}{2} \int\int \frac{n(\boldsymbol{r}, t) n(\boldsymbol{r}', t)}{|\boldsymbol{r} - \boldsymbol{r}'|} \, \mathrm{d}^3 r \, \mathrm{d}^3 r' + E_{\mathrm{xc}}[n] - \int V_{\mathrm{xc}}[n] n(\boldsymbol{r}, t) \, \mathrm{d}^3 r. \quad (25)$$

The first term in equation (24) is the kinetic energy of the ions, which are treated classically. The following terms can be easily derived from the TDDFT action functional in the Kohn–Sham representation, if one assumes that the XC contributions are local in time (see [29] for details).

In order to derive an efficient numerical scheme, we again make use of an expansion of equation (24) with respect to small density fluctuations δn around a suitable reference density n_0, $n = n_0 + \delta n$, described in section 2.1 for the time-independent formulation of DFTB theory. The result up to second order reads

$$\mathcal{L}(|\Psi_i\rangle, \boldsymbol{R}_\alpha) = \sum_{\alpha} \tfrac{1}{2} M_\alpha \dot{\boldsymbol{R}}_\alpha^2 - \sum_i n_i \langle \Psi_i | H[n_0] - \mathrm{i}(\overleftrightarrow{\mathrm{d}/\mathrm{d}t}) | \Psi_i \rangle - E_{\mathrm{rep}} + \mathcal{O}(\delta n^2). \quad (26)$$

In contrast to our approach in earlier sections, here we do not take the second-order contributions into account. This was found to be a good approximation for systems with

little charge transfer such as homonuclear clusters (see also [43] for a more detailed discussion of this point). However, to cover a broader range of systems, the next term in the expansion in equation (26) has also to be included, which results in a numerically complex scheme. Efforts to address this task are currently under way.

Requiring the action $\int \mathcal{L}\,\mathrm{d}t$ of equation (26) to be stationary with respect to variations in $\boldsymbol{R}_\alpha$ and ψ_j finally leads to coupled equations of motion for electrons and ions. After expanding the TD Kohn–Sham orbitals in our LCAO basis (section 2.4.1) $\Psi_i(t) = \sum_\mu b_\mu^i(t)\varphi_\mu(\boldsymbol{r} - \boldsymbol{R}_\alpha(t))$, they read

$$\begin{aligned}
\dot{b}_{\nu i}(t) &= -\sum_{\mu\gamma}(S^{-1})_{\nu\gamma}\left[\mathrm{i}H_{\gamma\mu} + \left\langle\phi_\gamma\left|\frac{\mathrm{d}}{\mathrm{d}t}\phi_\mu\right.\right\rangle\right]b_{\mu i} \\
\boldsymbol{F}_\alpha &= -\sum_{i\mu\nu\gamma\delta} n_i b_\mu^{i*} b_\nu^i \left\{\frac{\mathrm{d}H_{\mu\nu}}{\mathrm{d}\boldsymbol{R}_\alpha} - \left\langle\frac{\mathrm{d}\phi_\mu}{\mathrm{d}\boldsymbol{R}_\alpha}\right|\phi_\gamma\right\rangle S^{-1}_{\gamma\delta}H_{\delta\nu} - H_{\mu\gamma}S^{-1}_{\gamma\delta}\left\langle\phi_\delta\left|\frac{\mathrm{d}\phi_\nu}{\mathrm{d}\boldsymbol{R}_\alpha}\right.\right\rangle\right\} - \frac{\mathrm{d}E_{\mathrm{rep}}}{\mathrm{d}\boldsymbol{R}_\alpha}.
\end{aligned} \tag{27}$$

These are the time-dependent Kohn–Sham (TD-KS) equations of DFTB theory in the LCAO basis representation, explicitly accounting for the time propagation of the Kohn–Sham eigenstates in coupling to the motion of the atomic framework, and a generalized Ehrenfest theorem giving the forces on the nuclei. Both equations clearly represent a non-adiabatic approach to MD, accounting for complex coupling of ground-state and excited-state potential energy surfaces.

The derivation given here provides an extension to two earlier contributions to this field. Equations of motion which are similar to equation (27) were given by Graves and Allen for an empirical orthogonal TB scheme [47, 48] and by Saalmann and Schmidt [50] for the special case of not explicitly TD Hamiltonians.

Recently Todorov showed [49] that for an incomplete basis set the force equation (27) has to be augmented by additional terms. These corrections contain the nuclear velocities and should become important e.g. in the simulation of high energy collisions. Interestingly, neglect of the force corrections does not affect the conservation of energy, but the conservation of momentum of the combined system of electrons and nuclei.

Up to now, we did not specify how the external radiation field is included in the Hamiltonian. This is done via minimal coupling ($\boldsymbol{p} \to \boldsymbol{p} - (e/c)\boldsymbol{A}$), where $\boldsymbol{A}$ is the vector potential. Following Graf and Vogl [51], the TD Hamiltonian may be rewritten as

$$H\left(\boldsymbol{r}, \boldsymbol{p} - \frac{e}{c}\boldsymbol{A}(\boldsymbol{r}, t)\right) = \exp\left[\frac{\mathrm{i}e}{\hbar c}\int^{r}\boldsymbol{A}(\boldsymbol{s}, t)\,\mathrm{d}\boldsymbol{s}\right]H(\boldsymbol{r}, \boldsymbol{p})\exp\left[-\frac{\mathrm{i}e}{\hbar c}\int^{r}\boldsymbol{A}(\boldsymbol{s}, t)\,\mathrm{d}\boldsymbol{s}\right]. \tag{28}$$

Here

$$\int^{r}\boldsymbol{A}(\boldsymbol{s}, t)\,\mathrm{d}\boldsymbol{s} \tag{29}$$

denotes a line integral over the vector potential. For wavelengths in the optical range, the vector potential is essentially constant over molecular dimensions. Taking advantage of this, the matrix elements of $H(\boldsymbol{r}, \boldsymbol{p} - (e/c)\boldsymbol{A}(\boldsymbol{r}, t))$ in the LCAO basis can be related to the unperturbed ones, equation (4), known already:

$$H_{\mu\nu}(t) = \exp\left[\frac{\mathrm{i}e}{\hbar c}(\boldsymbol{R}_\alpha - \boldsymbol{R}_\beta)\boldsymbol{A}(t)\right]H^0_{\mu\nu} \qquad \mu \in \alpha,\ \nu \in \beta. \tag{30}$$

Equation (30) is in principle valid for arbitrarily strong TD fields, consistent with the two-centre approximation and explicitly respects gauge invariance.

Finally, to solve the coupled equations of motion, equation (27), we use the velocity Verlet algorithm for the force equation, and a new algorithm based on the Cayley representation [52] to integrate the TD-KS equations [43].

As an illustrative application of the method, we briefly report in section 4 results on the vibrational excitation of buckminsterfullerene C_{60} due to femtosecond laser pulses.

2.4. Practical realization

2.4.1. LCAO basis and atomic reference density. The pseudo-atomic basis functions $|\varphi_\mu\rangle$ are Slater-type atomic orbitals:

$$\varphi_\mu(\boldsymbol{r}) = \sum_\zeta \sum_i (a_{\zeta i} r^{l+i}) \mathrm{e}^{-\zeta r} Y_{lm}\left(\frac{\boldsymbol{r}}{r}\right), \tag{31}$$

where l and m are the angular momentum and the magnetic quantum numbers associated with the orbital μ, respectively. Extensive tests have shown that five different values of ζ and $i = 0, 1, 2, 3$ form a sufficiently accurate basis set [53].

With this basis set we solve the Kohn–Sham equation for a spherically symmetric spin-unpolarized neutral atom self-consistently:

$$\left[\hat{T} + V_{\mathrm{eff}}^{\mathrm{at}}(r) + \left(\frac{r}{r_0}\right)^2\right]\varphi_\mu(\boldsymbol{r}) = \varepsilon_\mu \varphi_\mu(\boldsymbol{r}). \tag{32}$$

Here a harmonic contraction potential $(r/r_0)^2$ has been added, as introduced by Eschrig [53,54], to form a more efficient basis set for molecular and solid-state systems. The parameter r_0 is chosen to be about 1.85 times the atomic covalent radius [23] and $V_{\mathrm{eff}}^{\mathrm{at}}$ is the effective pseudo-atomic potential.

From this procedure we obtain for each atom type optimized atomic basis sets $\{\varphi_\mu\}_\mu$ and atomic densities n_α^0 which are used to calculate the matrix elements of the zeroth-order Hamiltonian $H_{\mu\nu}^0$ in a two-centre approximation, as discussed in section 2.1.

2.4.2. Determination of $\gamma_{\alpha\alpha}$. The total-energy expression of SDFTB reads in the atomic case

$$E_{\mathrm{at}}^{\mathrm{SDFTB}} = \sum_{\sigma=\uparrow,\downarrow} \sum_i^{\mathrm{occ}} n_{i\sigma}\varepsilon_i + \tfrac{1}{2}\gamma_{\alpha\alpha}\,\Delta q^2 + \frac{1}{2}\sum_l \sum_{l'} p_l p_{l'} W_{ll'}. \tag{33}$$

In SDFTB the electron density $n(\boldsymbol{r})$ is approximated by the Mulliken populations q. Differentiating equation (33) twice yields then

$$\frac{\partial^2 E_{\mathrm{at}}^{\mathrm{SDFTB}}}{\partial n^2} \approx \frac{\partial^2 E_{\mathrm{at}}^{\mathrm{SDFTB}}}{\partial q^2} = \gamma_{\alpha\alpha}. \tag{34}$$

To obtain the atomic constant $\gamma_{\alpha\alpha}$, we also differentiate the atomic total-energy expression of DFT. Under the assumption of fixed orbital shapes, the derivative with respect to the density can be reduced to a derivative with respect to the occupation numbers n_i. Using Janak's theorem [55] yields

$$\frac{\partial^2 E_{\mathrm{at}}^{\mathrm{DFT}}}{\partial n^2} \approx \frac{\partial^2 E_{\mathrm{at}}^{\mathrm{DFT}}}{\partial n_i^2} = \frac{\partial \varepsilon_i}{\partial n_i}. \tag{35}$$

In the case where i is the highest occupied molecular orbital (HOMO), the derivative $\partial\varepsilon_{\mathrm{HOMO}}/\partial n_{\mathrm{HOMO}}$ is associated with the Hubbard U of atom type α, U_α, which in turn is associated with the ionization potential I_α and the electron affinity A_α of the atom, $U_\alpha \approx I_\alpha - A_\alpha$.

Requiring equality of the results of equations (34) and (35), we have the identity

$$\gamma_{\alpha\alpha} = \frac{\partial \varepsilon_{\mathrm{HOMO}}}{\partial n_{\mathrm{HOMO}}} = U_\alpha. \tag{36}$$

By the construction of the expression $\gamma_{\alpha\beta}$, the atomic Hubbard Us also enter in the interatomic contributions [22].

2.4.3. Determination of $W_{\alpha ll'}$. The universal atomic constants $W_{\alpha ll'}$ can be calculated for free atoms by taking second derivatives of the DFT and SDFTB total-energy expressions with respect to the magnetization density.

Within SDFTB theory the magnetization density is approximated by Mulliken spin populations; see equation (7). Differentiation of the total-energy expression in the atomic case, equation (33), leads then to the equation

$$\frac{\partial^2 E_{\mathrm{at}}^{\mathrm{SDFTB}}}{\partial \mu_l \, \partial \mu_{l'}} \approx \frac{\partial^2 E_{\mathrm{at}}^{\mathrm{SDFTB}}}{\partial p_l \, \partial p_{l'}} = W_{ll'} \tag{37}$$

for the universal constant $W_{ll'}$ of an atom α of a specific type.

In the DFT case one obtains by applying Janak's theorem [55]

$$\frac{\partial^2 E_{\mathrm{at}}^{\mathrm{DFT}}}{\partial \mu_l \, \partial \mu_{l'}} \approx \frac{1}{4}\left(\frac{\partial \varepsilon_{l\uparrow}}{\partial n_{l'\uparrow}} - \frac{\partial \varepsilon_{l\uparrow}}{\partial n_{l'\downarrow}} - \frac{\partial \varepsilon_{l\downarrow}}{\partial n_{l'\uparrow}} + \frac{\partial \varepsilon_{l\downarrow}}{\partial n_{l'\downarrow}}\right) = \frac{1}{2}\left(\frac{\partial \varepsilon_{l\uparrow}}{\partial n_{l'\uparrow}} - \frac{\partial \varepsilon_{l\uparrow}}{\partial n_{l'\downarrow}}\right), \tag{38}$$

where the relations $n_{l\uparrow} = \frac{1}{2}(n_l - \mu_l)$ and $n_{l\downarrow} = \frac{1}{2}(n_l + \mu_l)$, assuming fixed orbital shapes, have been used. Then the $\varepsilon_{l\uparrow}$ and $\varepsilon_{l\downarrow}$ are the Kohn–Sham eigenvalues while the $n_{l\uparrow}$ and $n_{l\downarrow}$ are the occupation numbers. The rightmost part is obtained via symmetry constraints imposed by the reference point of the spin-unpolarized atom.

Finally, we have, under the requirement that the results of equation (37) and equation (38) are equal,

$$W_{ll'} = \frac{1}{2}\left(\frac{\partial \varepsilon_{l\uparrow}}{\partial n_{l'\uparrow}} - \frac{\partial \varepsilon_{l\uparrow}}{\partial n_{l'\downarrow}}\right). \tag{39}$$

The $W_{ll'}$ can now be calculated for every atom type.

3. Large systems

Although the DFTB approach is about 2–3 orders of magnitude faster than the DFT one, the limits of modern computers are reached when considering long MD simulation times of more than several 100 ps and/or large systems containing more than 500 atoms. In principle, there are three strategies for going beyond these thresholds: parallelization, linear scaling algorithms and combination of different methods. All three approaches have their merits and also combinations are possible. Which one to choose depends on the special problem of interest.

3.1. Parallelization

The problems described by equations (9)–(11) and (13) scale with N^3, where N is the number of basis functions, and are therefore computationally expensive. These equations can be implemented in a straightforward manner for parallel machines. Advantage can be taken by the use of special linear algebra packages (Scalapack, PBLAS) which optimize data transport between processors in parallel computers [56–59]. For details, see [26].

3.2. $\mathcal{O}(N)$ methods

The computational cost of the SCC-DFTB method is determined by the diagonalization of the Hamiltonian matrix, which exhibits $\mathcal{O}(N^3)$ (cubic) scaling with increasing system size N. Linear scaling ($\mathcal{O}(N)$ scaling) can be achieved by circumventing the matrix diagonalization in the solution of the generalized eigenvalue problem. In the last decade, there have been

several proposals for a realization of an $\mathcal{O}(N)$-like scaling. For a more detailed discussion of the different approaches, see e.g. [60–63] and [64].

A simple $\mathcal{O}(N)$ approach was introduced by Yang with the so-called DAC scheme [65, 66]. The algorithm was then simplified by Yang and Lee introducing a density matrix formulation [66]. For systems where the density matrix is localized in real space, it can be constructed from local contributions. Practically, the system of interest is divided into subsystems, and the total density matrix is projected onto the density matrices of the subsystems. The eigenvalue problems of the subsystems are solved separately instead of solving the problem for the total system. The occupation numbers of the orbitals of the subsystems are then determined on the basis of the Fermi energy in order to obtain the total number of electrons of the entire system. For large systems, the size of the subsystems is independent of the total system size, and the number of subsystems increases linearly with the overall system size, which leads to the desired $\mathcal{O}(N)$ scaling. Recently, the DFTB method has been implemented in the DAC algorithm [67, 68]. For small systems, the DAC-DFTB method is computationally more expensive than the conventional diagonalization; it becomes more efficient only at a certain 'crossover' point. For biological systems like peptides and proteins, which consist dominantly of O, N and C atoms and about 40% hydrogen atoms, this crossover point is reached for system sizes of roughly 200 atoms (all atoms described in the DFTB minimal basis). As a first benchmark, we considered the crambin protein, which contains 639 atoms. Using conventional diagonalization techniques, the evaluation of an energy gradient takes about 15 min on a DEC Alpha EV6 machine, whereas the DAC method needs about 1 min for the same task. Therefore, a complete geometry optimization of this molecule can be performed a few several hours of laboratory clock time. However, the structures of biological molecules are seldom of interest under dry conditions. Further, to address questions about conformational stability and dynamics of macromolecular structures, simple geometry optimizations are of no further use and MD trajectories on the nanosecond timescale have to be evaluated. To achieve long MD trajectories including a large number of water molecules to account for solvation, further technical improvements have to be implemented.

3.3. QM/MM

Another route to large systems consists in the combination of a quantum mechanical method with an empirical force field. The idea behind the combined quantum mechanics/molecular mechanics (QM/MM) force-field methods is to describe a part of the molecule quantum mechanically and the rest of the system within the computationally much faster empirical force-field approach.

In this approach, the total energy is usually written as

$$E_{\mathrm{tot}} = E_{\mathrm{QM}} + E_{\mathrm{MM}} + E_{\mathrm{QM-MM}}, \tag{40}$$

where E_{QM} is the energy of the QM part of the subsystem, represented by the SCC-DFTB energy (equation (10)), E_{MM} is the energy of the MM subsystem, given by the energy function of the empirical force field, and $E_{\mathrm{QM-MM}}$ describes the coupling of the two subsystems.

If the boundary of the QM and MM regions intersects a covalent bond, the combination of these methods is not straightforward. Several suggestions have been made as regards how to tackle this problem. A popular approach is the so-called link-atom approach, where the quantum system is saturated with a fictitious atom for the QM calculation only, while the bond across the QM/MM boundary is modelled by the bonding interaction of the empirical force field. QM/MM approaches have been reviewed recently [69, 70], and we will not discuss details of their implementation. We will just present the main ideas for the SCC-DFTB/MM coupling [71, 72].

$E_{\mathrm{QM-MM}}$ consists of Coulomb and vdW interactions between the two subsystems. The vdW interaction is modelled by the interaction terms present in the empirical force-field method, while the Coulomb term is approximated by the interactions of the point charges between the subsystems, where the QM charges are given by the Mulliken charges Δq_α of the SCC-DFTB method:

$$E_{\mathrm{QM-MM}} = -\sum_{\alpha\epsilon\mathrm{QM},\beta\epsilon\mathrm{MM}} \frac{\Delta q_\alpha\, Q_\beta}{R_{\alpha\beta}} + E_{\mathrm{vdW}}. \tag{41}$$

The total energy is

$$E_{\mathrm{tot}} = E_{\mathrm{QM}} + E_{\mathrm{MM}} - \sum_{\alpha\epsilon\mathrm{QM},\beta\epsilon\mathrm{MM}} \frac{\Delta q_\alpha\, Q_\beta}{R_{\alpha\beta}} + E_{\mathrm{vdW}}. \tag{42}$$

We have tested this method extensively for H-bonded compounds, where one molecule is treated quantum mechanically and the other is treated with the force-field method. The results are very promising: geometries and energies compare well with higher-level calculations and the relative ordering of the energies of several conformers is well reproduced [72]. Also proton-transfer barriers have been investigated in detail within the QM/MM framework for triosephosphate isomerase (TIM) enzyme [73]. The results have been compared with full DFT calculations from a previous study on this system and have been found to be in an excellent agreement. Further, QM/MM MD simulations have been performed to study the stability of protein alpha helices in aqueous solution. For this purpose, the peptides have been treated within QM, while the water molecules were simulated within the MM framework.

3.4. Parallel $\mathcal{O}(N)$ QM/MM method

In order to simulate the crambin protein in aqueous solution over a longer timescale, we combined the $\mathcal{O}(N)$ algorithm with the QM/MM methodology, where the crambin molecule can be treated within QM, and the solvent water molecules within MM [67]. This allows one to centre the protein in a cubic box, surrounded by about 2400 water molecules.

On a DEC Alpha machine, a picosecond of dynamics would take about a day run time. We therefore used a parallel version of the DAC QM/MM method, where we were able to achieve about 10 ps dynamics per day using 16 processors of an IBM-SP3 machine. In total, a simulation for 350 ps has been performed. The high-resolution crystal structure was better reproduced than in similar simulations using empirical force fields for the whole system, i.e. for crambin and the solvent. In particular, some non-local charge transfer between the termini of the protein has been found; this is excluded by construction in pure empirical force-field simulations.

4. Properties

4.1. Vibrational spectra

For the calculation of vibrational spectra of molecules and solids within the harmonic approximation, the dynamical matrix is needed, i.e. the second derivatives of the total energy with respect to the atomic coordinates ($\boldsymbol{R}_\alpha$): $\partial^2 E/\partial \boldsymbol{R}_\alpha\, \partial \boldsymbol{R}_\beta$. Within the DFTB method the forces on the atoms ($-\partial E/\partial \boldsymbol{R}_\alpha$) can be calculated analytically (equation (13)), whereas an analytical calculation of the second derivatives of the energy is more involved. Therefore the dynamical matrix is calculated numerically by means of finite differences of the forces. Diagonalization of the dynamical matrix gives then the vibrational eigenmodes (ω_i) and the corresponding eigenvectors. The intensities of infrared (IR) spectra (I_i) of the vibrational

eigenmodes (ω_i) can be obtained from the derivative of the calculated dipole moment (μ) with respect to the corresponding normal coordinate (Q_i): $I_i \sim |\mathrm{d}\mu/\mathrm{d}Q_i|^2$. For Raman intensities (I_{Raman}) the derivative of the polarizability (α) is required: $I_{\mathrm{Raman}} \sim |\mathrm{d}\alpha/\mathrm{d}Q_i|^2$. Up to now, we used a bond polarization model for the calculations of the polarizabilities as originally proposed by Snoke and Cardona [74].

We have tested frequencies of a series of 33 O, N, C and H containing organic molecules yielding about 6% mean absolute deviation of vibrational frequencies from the experiment [71]. On average, bond-stretching frequencies are slightly overestimated with respect to experiment [25]. The largest errors occur in the low-frequency range, implying that torsional barriers are not described with the same accuracy as bond-stretching potentials. Similar results have been found for sulphur-containing molecules [75].

Placing special emphasis on the spectra of fullerene derivatives, we have contributed with these calculations to the identification of the structural oligomer patterns of such systems [25, 76–78].

Recently, we also studied the vibrational frequencies and IR and VCD intensities of NA-LA-NMA with the SCC-DFTB method, in comparison with HF, B3LYP and MP2 calculations [79]. In [79], we have calculated the IR and VCD intensities at the HF, DFT and MP2 levels of theory. To estimate the intensities at the SCC-DFTB level, we used an SCC-DFTB-DFT hybrid approach. Ground-state geometries and second energy derivatives have been calculated with SCC-DFTB theory and the dipole derivatives and VCD tensors at the B3LYP level of theory in the SCC-DFTB geometry. The SCC-DFTB vibrational frequencies have been shown to agree very well with those of the higher-level calculations, and the intensities estimated with the hybrid approach compare satisfactorily with those of the higher-level calculations [79] for the two conformers investigated, C_7^{eq} and C_5^{ext}.

This good agreement motivated us to calculate the IR intensities fully at the SCC-DFTB level of theory. We used the derivatives of the SCC-DFTB dipole moments with respect to the atomic coordinates as an approximate way to calculate the IR intensities [27]. The dipole moments are calculated from Mulliken charges, which neglects the intra-atomic charge-density distribution but is computationally very efficient. The spectra are reproduced only qualitatively in this way, but the errors follow a certain trend. The high-intensity modes are overestimated in their intensity compared to the low-intensity modes. A scaling of intensities according to their amount leads to a good agreement with the more sophisticated calculations [27].

Besides in the calculations of IR and Raman spectra of molecular systems, the DFTB method has also been applied for the calculation of the vibrational (phonon) spectra of crystalline and amorphous solids and solid surfaces [80, 81]. For instance, the structure and elastic properties of amorphous silicon carbon nitride films, depending on their carbon content, have been studied in detail [82]. These amorphous films were deposited by ion-beam sputtering in such a way that a graphite sheet covered with a smaller silicon wafer at the centre was further covered by a smaller SiC film and was used as the target for a N_2^+ beam with a 45° angle of incidence. By adjusting the sputter target and the N_2^+ beam voltage, films of different compositions and carbon contents were deposited on Si(100) and fused silica substrates. In this study, besides various other experimental methods for the determination of the structural properties and chemical bonding conditions, Fourier-transform infrared (FTIR) spectroscopy has been applied to obtain the IR intensities to investigate these films.

To model the a-SiC_xN_y films, MD simulations for 224–240 atoms enclosed within a simple cubic periodic supercell with fixed volume according to the mass density and with the same compositions of Si, C and N as the sputtered films have been performed. To simulate the experimental situation as closely as possible, the initial structures for the MD simulation were arranged corresponding to the adjustment of the sputter target described before. Therefore,

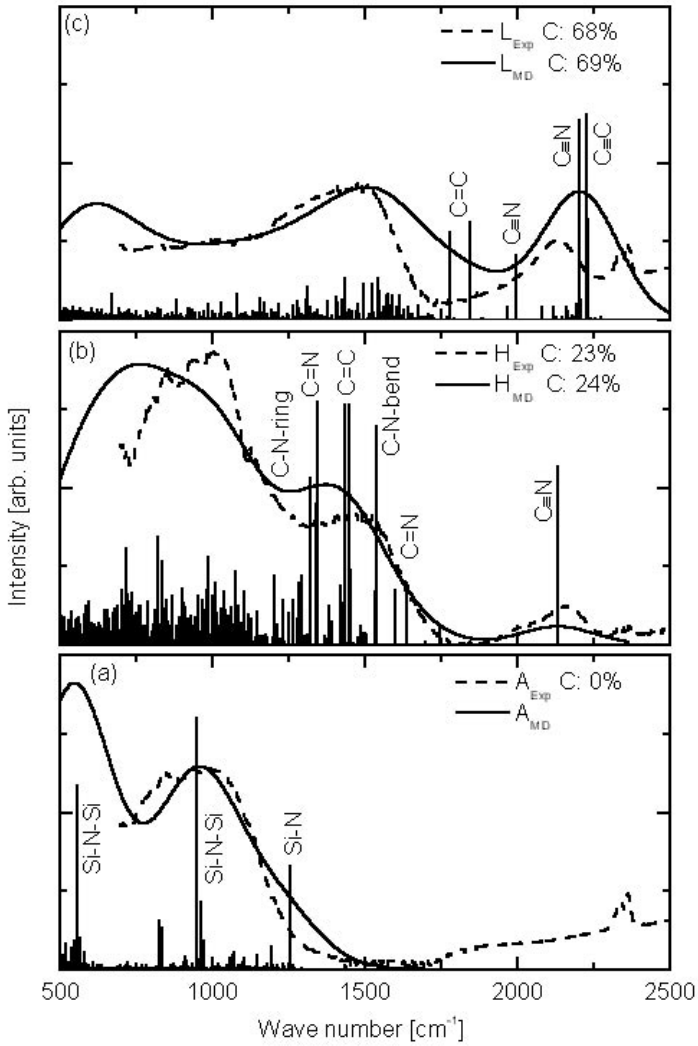

Figure 2. IR spectra obtained experimentally (dashed line) and by MD simulation (solid line) for amorphous (*a*) $Si_{47}N_{53}$, (*b*) $Si_{42}C_{24}N_{34}$ and (*c*) $Si_9C_{69}N_{22}$. The simulated spectra consist of overlapping delta peaks which are also shown. These were Gaussian broadened for adjustment to the experimental conditions of the FTIR spectroscopy [82].

for example, the nitrogen atoms were inserted randomly, simulating the N_2^+ beam. As the MD regime for the structure formation, the initial structures were first heated from 300 to 4000 K in 1 ps with linearly increasing temperature. Then, they were equilibrated for 1 ps at 4000 K and after that cooled down to 300 K in 1 ps. Finally, the models were equilibrated at 300 K for another picosecond and then relaxed with a conjugate gradient algorithm.

The experimental and calculated IR spectra of three of these amorphous films are shown in figure 2. From the calculations, delta peaks were obtained for the IR intensities. These have been Gaussian broadened to adapt to the experimental conditions of the FTIP spectroscopy for better comparison. One can see that, except at wavenumbers below 700 cm^{-1}, where the sensitivity of the detector used in the experimental FTIR investigation is low, the broadened

theoretical and the experimental spectra show a reasonable agreement as regards peak positions and relative peak heights. The double peak at 2350 cm^{-1} that is only present in the experimental IR spectra is due to CO_2 absorption in the ambient air, and is therefore not characteristic for the films. With the calculation of the spectra and a detailed geometrical analysis of the MD models, it has been possible to provide detailed information about the chemical bonding situation. Therefrom, it could be seen that with increasing carbon content the formation of C=C, C=N, C≡C and C≡N bonds increases together with a decrease of the total coordination number of silicon and carbon. Thus, it could be shown that this formation of double and triple bonds together with an increasing number of terminating nitrogen atoms upon increase of the carbon content are responsible for the degradation of the sp^3 network of the material, and therefore for a lower Young's modulus and density.

It should also be mentioned that the DFTB method allows one to calculate vibrational spectra (vibrational density of states $f(\omega)$) beyond the harmonic approximation via a Fourier transformation of the velocity autocorrelation function ($C(t)$), obtained from MD simulations:

$$C(t) = \frac{\sum_k^M \langle \boldsymbol{v}_k(t)\boldsymbol{v}_k(0)\rangle}{\sum_k^M \langle \boldsymbol{v}_k(0)\boldsymbol{v}_k(0)\rangle}, \tag{43}$$

where $\boldsymbol{v}_k(t)$ is the velocity of the kth atom at time t, M is the number of atoms in the system:

$$f(\omega) = \frac{1}{2\pi}\int_0^\infty C(t)\exp(\mathrm{i}\omega t)\,\mathrm{d}t. \tag{44}$$

Such treatment has been applied e.g. for the interpretation of vibrational spectra of endohedral fullerenes [83].

4.2. Optical spectroscopy

Test calculations for optical excitation energies and related spectra on a set of small organic molecules showed a good agreement of calculations within the γ-approximation (section 2.2) with full TDDFRT calculations for low-lying singlet states, where mean absolute errors of 0.38 and 0.36 eV, respectively, were found with respect to experiment. The results for triplet excitations were less convincing. We obtained an error of 0.64 eV for our approach, while TDDFRT performed much better giving an error of 0.37 eV. However, general trends like chain-length-induced red-shifts in polyenes are correctly described for both types of excitation. This is reflected in figure 3 where results for the polyacene series ($C_{4n+2}H_{2n+4}$) are shown in comparison with TDDFRT and experimental values.

As a further test of our method we calculated the absorption spectrum of several sulphur–organic compounds. These systems, among them in particular the thiophene-based materials, are becoming of increasing technological importance since they combine ease of processibility with tunable optical properties and high quantum yield.

An overview of the results is given in figure 4 where all the excitations calculated have been accumulated in one correlation plot together with results obtained by Fabian [38] for TDDFRT and the INDO/S method. As in the case of pure organic systems, the γ-approximation shows a balanced performance over the whole test set close to the accuracy of the more time-demanding TDDFRT scheme. This transferability over different bonding situations can be traced back to the neglect of empirical parameters. In contrast, the parametrized INDO/S method, although very precise for most of the compounds, fails for some of the transitions with errors as high as 1.97 eV.

[4] Calculations were performed for the following molecules: thioacetone, 3-methylthiocyclopentenone, thiobenzaldehyde, 1, 2-dithiole-3-thione, thiophene, benzthiet, thiophenol, cyclopenta[*c*]thiapyran, 1-thiaphenalene, 1, 2-dithiin, 1, 2-dithiane, naphtho[1, 8-*cd*]dithiol, 3, 4-dimethylenethiophene, thiosulphine and thiophene *S*-dioxide.

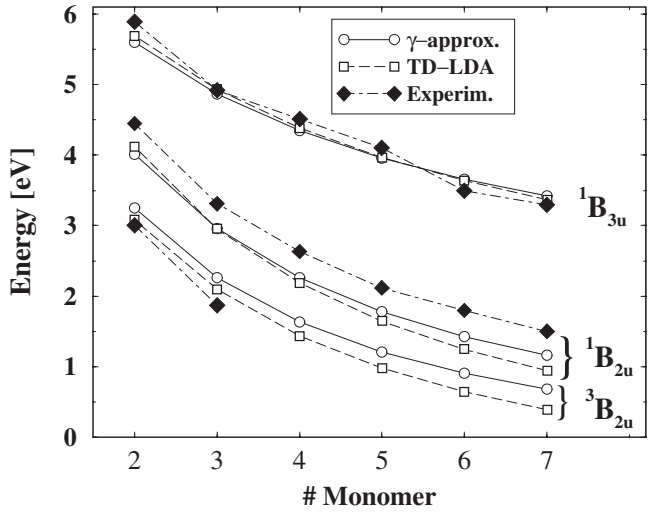

Figure 3. Comparison of the lowest singlet and triplet as well as the most intense singlet excitation energy for the polyacenes as obtained from the γ-approximation, TDDFRT with a LDA XC functional and experiment. The values for the latter two were taken from [84].

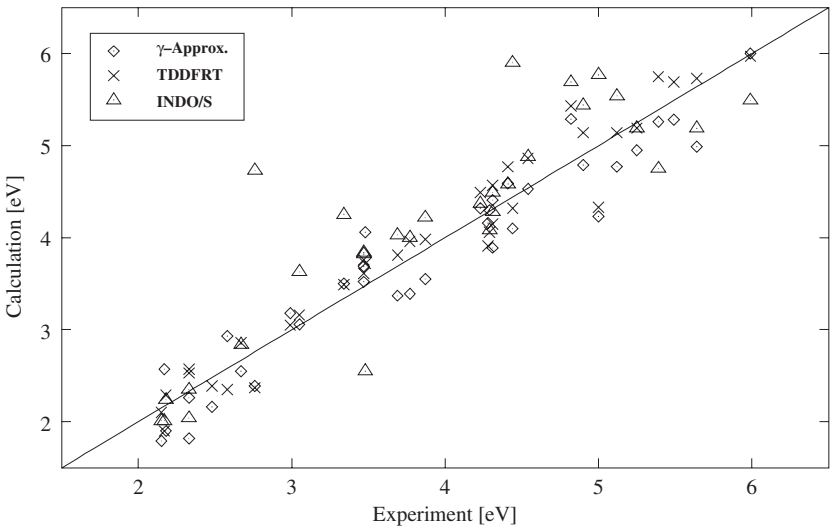

Figure 4. A correlation plot of calculated singlet excitation energies of several sulphur-containing molecules[4] versus experiment. The TDDFRT and INDO/S results as well as the experimental values were taken from [38].

4.3. Pump–probe ultrashort-time spectroscopy

With the advent of subpicosecond laser sources it became possible to time resolve the dynamics of systems on very short timescales, supplementing the information conventional optical spectroscopy can provide us with. Strongly localized in time, these short pulses exhibit a broad frequency spectrum which leads to a coherent excitation of many vibrational states. This effect is manifested in quantum beats of the reflectivity or transmission, which may

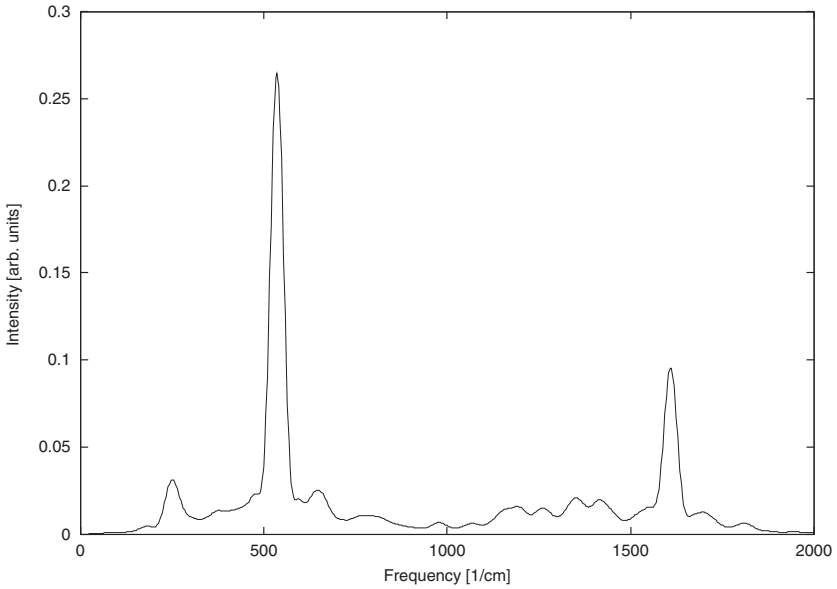

Figure 5. The result of a MD simulation of C_{60}. The cluster was subjected to a Gaussian-shaped pulse of 12 fs duration with a carrier frequency of 2 eV/$\hbar$ and a vector potential of 1.13 G cm. After the end of the pulse the simulation was continued for 1 ps. Shown here is the Fourier transform of the velocity autocorrelation which was calculated from the sampled data. For details, see [43]. The peak at $\approx$500 1 cm^{-1} corresponds to the breathing mode of the cluster, while the one at $\approx$1600 1 cm^{-1} is identified as the pentagonal pinch mode.

be resolved with a pump–probe experimental set-up. Interestingly, only totally symmetric modes are observed under usual experimental conditions [85]. This holds also for C_{60}, where according to Dexheimer *et al* [86] irradiation of the sample with a 12 fs pulse centred at 2 eV leads to a dominant excitation of the two A_g modes of the molecule. This finding agrees very well with simulations that we performed on this system (see figure 5). However, for a lower fluence of the exciting pulse we obtain a much richer pattern (figure 6). Now, modes of lower symmetry also appear and the spectrum closely resembles the one obtained from Raman measurements, where the pentagonal pinch mode is much stronger than the breathing mode [87]. According to analytical theories [85, 88] it is expected that only those vibrations which possess a long period compared to the duration of the pulse are impulsively excited. This prediction is confirmed by our calculations. In figure 7, results of a simulation with same fluence as in figure 5 but doubled pulse duration show a diminishing of the high-frequency pentagonal pinch mode. To sum up, just by changing one of the parameters of the pulse, the vibrational excitation is radically changed, which may be viewed as another example of coherent control.

4.4. Electron paramagnetic resonance, EPR

In the general LCAO case the isotropic hyperfine-coupling constants (hfccs) can be calculated from the expression [89]

$$a_{\mathrm{iso}}^{(\mathrm{N})} = \frac{4\pi}{3} g\beta\gamma_{\mathrm{N}}\hbar\langle S_z\rangle^{-1} \sum_{\mu\nu} \rho_{\mu\nu}\langle\varphi_\mu(\boldsymbol{r}-\boldsymbol{R}_\alpha)|\delta(\boldsymbol{r}-\boldsymbol{R}_{\mathrm{N}})|\varphi_\nu(\boldsymbol{r}-\boldsymbol{R}_\beta)\rangle. \quad (45)$$

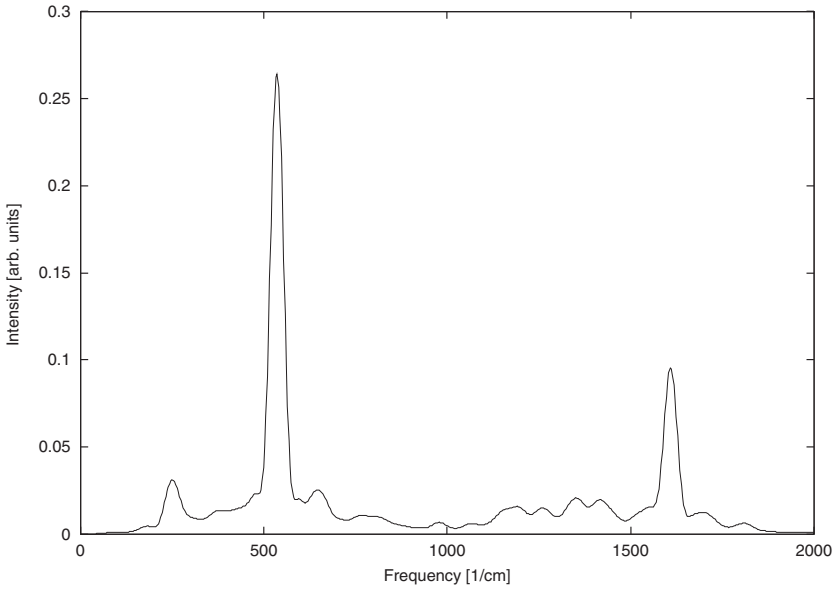

Figure 6. Spectral density from a simulation with same pulse parameters as in figure 5 apart from the vector potential which was 0.08 G cm in this case.

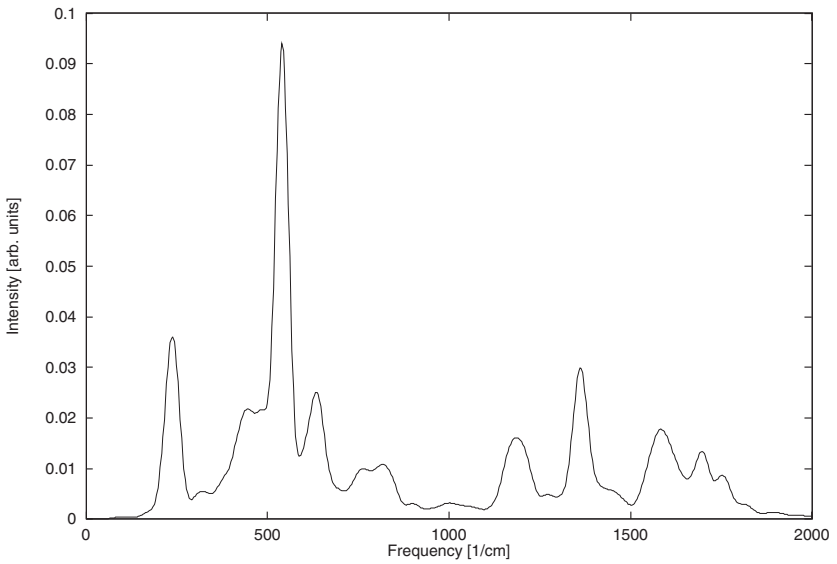

Figure 7. Spectral density from a simulation with the same fluence as in figure 5 but doubled pulse duration.

β, γ_{N} and g are the Bohr magneton, the gyromagnetic ratio of nucleus N and the electronic g-factor of the free electron, respectively, and $\langle S_z \rangle$ is the expectation value of the spin operator S_z. The expression $\langle \varphi_\mu(\boldsymbol{r} - \boldsymbol{R}_\alpha)|\delta(\boldsymbol{r} - \boldsymbol{R}_{\mathrm{N}})|\varphi_\nu(\boldsymbol{r} - \boldsymbol{R}_\beta)\rangle$ gives the density of the basis functions at the nucleus N and is associated with the spin-density matrix element $\rho_{\mu\nu} = \sum_i^{\mathrm{occ}} (n_{i\uparrow} c_{\mu i}^{\uparrow} c_{\nu i}^{\uparrow} - n_{i\downarrow} c_{\mu i}^{\downarrow} c_{\nu i}^{\downarrow})$.

Table 1. Isotropic hfccs (mT) of a stilbene radical anion; for the atom labels see figure 9. In this case the AM1 optimized geometry was used [91]. Reproduced with permission of the PCCP Owner Societies.

Number	Experiment [96]	DFT calculation [96]	SDFTB calculation
1	−0.26	−0.22	−0.22
2	0.08	0.06	0.02
3	−0.38	−0.36	−0.36
4	0.04	0.02	0.02
5	−0.21	−0.18	−0.22
6a	0.66	0.70	0.61
6b	0.29	0.28	0.31
7	−0.04	−0.02	0.01

In our approximation the isotropic hfccs are calculated from the spin-density matrix elements ρ_{ss}^{N} of the s-functions centred on a particular atom N:

$$a_{\mathrm{iso}}^{(\mathrm{N})} = \langle S_z \rangle^{-1} \underbrace{\left(\frac{4\pi}{3} g\beta\gamma_{\mathrm{N}}\hbar |\varphi_{s\mathrm{N}}(\boldsymbol{R}_{\mathrm{N}})|^2 \right)}_{\text{constant}} \rho_{ss}^{\mathrm{N}}. \tag{46}$$

Here $|\varphi_{s\mathrm{N}}(\boldsymbol{R}_{\mathrm{N}})|^2$ is the density of the s-basis function at the nucleus. This was first introduced by Pople *et al* [90] for semi-empirical methods and is consistent with the various approximations in SDFTB theory [91], e.g. with the one-centre approximation for the spin polarization.

Extensive tests have been made for molecular and solid-state systems. These show quantitative agreement for molecules compared to experimental [90,92–94] and DFT [95,96] data.

Figure 8 shows a scatter-plot comparing DFT and SDFTB data to experiment for 168 protons in molecules containing C, O and N, demonstrating the applicability of the SDFTB approach. The distribution is centred and the deviations of DFT and SDFTB theory from experiment are similar. While the standard deviation of DFT from experiment is 0.179 mT, the standard deviation of SDFTB theory is, at 0.200 mT, of about the same value. This shows that SDFTB theory, which requires far less computational effort than DFT, provides a viable alternative to a fully self-consistent DFT calculation of isotropic hyperfine-coupling constants.

This may be further exemplified by means of the molecule depicted in figure 9. Table 1 gives the calculated and measured isotropic hyperfine-coupling constants. While the DFT calculation of the isotropic hfccs requires about 10 h computer time, only about 10 s are required with the SDFTB approach to obtain practically the same information.

The SDFTB approach is also capable of calculating isotropic hyperfine-coupling constants in solid-state systems as demonstrated for the vacancies in silicon and diamond and for a pair defect in SiC [91].

4.5. NMR

A crucial quantity in NMR spectroscopy is the nuclear magnetic shielding σ; it describes the screening of an external magnetic field ($\boldsymbol{H}_0$) at a nucleus N by the electrons. Strictly, it is a tensorial quantity, relating the external field strength $\boldsymbol{H}_0$ to the induced field $\boldsymbol{H}_{\mathrm{ind}}$ at N:

$$(\boldsymbol{H}_{\mathrm{ind}})_m = -\sum_{\beta} \sigma_{\alpha\beta} (\boldsymbol{H}_0)_n$$

with the Cartesian components m, n of the vectors. Use of density-functional-based schemes for magnetic properties requires some justification, as the Hohenberg–Kohn theorem does not

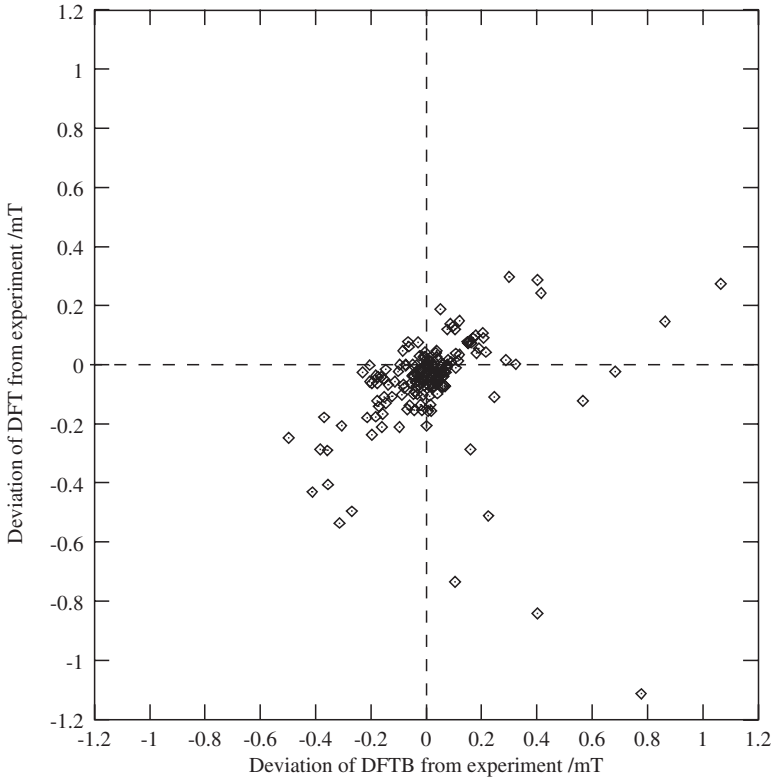

Figure 8. A plot of the deviations of DFT and SDFTB with respect to experimental data. Ideal agreement between experimental and calculated data would result in all points being at 0 mT [91]. Reproduced with permission of the PCCP Owner Societies.

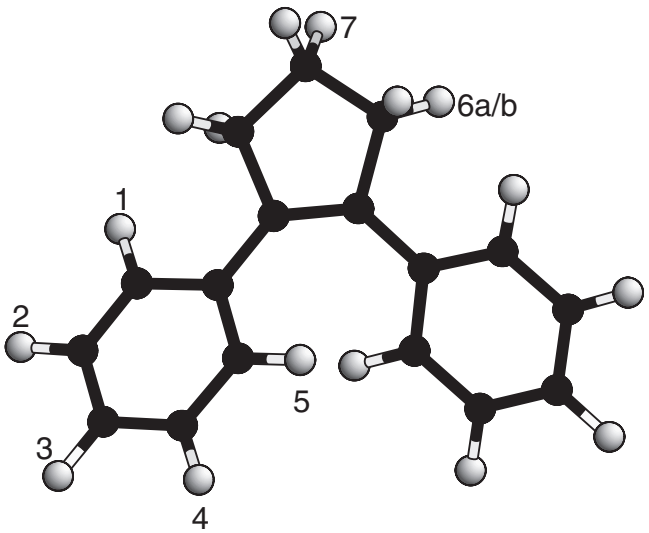

Figure 9. Atomic positions in a stilbene radical anion. For the isotropic hfccs see table 1. Hydrogen is white, carbon dark [91]. Reproduced with permission of the PCCP Owner Societies.

include vector potentials. Rajagopal and Callaway [97] proposed a relativistic generalized Hohenberg–Kohn theorem in terms of the 4-current density which leads to corresponding KS equations [98], and an expression for the nuclear magnetic shielding at point (nucleus N) in terms of the magnetic field derivative of the current density at that point can be derived. With some approximations [99, 100], the normal Rayleigh–Schrödinger expressions for the shielding can be recovered.

A perennial problem with calculation of magnetic properties is that of gauge origin. Given a choice of origin, the shielding splits into a sum of diamagnetic (expectation value) and paramagnetic (perturbed) contributions. Although in an infinite basis their sum is invariant, it can show strong dependence on the origin in a limited basis set. The solution that we adopted for diamagnetic molecules is the IGLO (individual gauge local orbitals) approach [101, 102] where the occupied molecular orbitals are first transformed to localized functions and for each LMO the centroid of charge is taken as the origin of vector potential. This choice has the advantage of reducing the magnitude of the paramagnetic contribution and hence minimizing sensitivity to the basis in the final computed result.

As an example for the application, the calculated structures of the stable isomers of the odd-membered fullerene C_{119} and the calculated ^{13}C NMR pattern of these structures are shown in figure 10 together with the experimental ^{13}C NMR spectrum [103]. The calculated pattern of the isomer A has a close match with the measured spectrum, whereas the patterns of the other isomers are considerably different i.e., the calculations can identify the isomer A as the species obtained experimentally by Gromov *et al* [103].

For a more detailed discussion, see [104]. Further practical realizations and applications are described in e.g. [105].

4.6. Scanning probe images, STM

Within the DFTB formalism the spatial charge-density distributions are explicitly available from the wavefunctions in real space. Plots of the charge density may be used in the analysis of surfaces and planar molecules to qualitatively reproduce the imaging process in scanning tunnelling microscopy (STM) [106]. This provides a coupling of the theoretical models to an experimental technique capable of resolving the atomic structure of surfaces on the same length scale as theory.

In the limit of an infinitesimally small tip, the tunnelling current I is proportional to the local density of states at the Fermi energy E_F, as shown by Tersoff and Hamann [107]:

$$I \propto n(\boldsymbol{r}, E_F) = \sum_i |\psi_i(\boldsymbol{r})|^2 \delta(\varepsilon_i - E_F). \tag{47}$$

By integration of the LDOS over an energy interval $(E) = (\varepsilon_{\min} \cdots \varepsilon_{\max})$ we obtain the spatial charge density as a sum over eigenstates:

$$n(\boldsymbol{r}) = \int_{(E)} n(\boldsymbol{r}, E) = \sum_{i_{\text{surf}}} n_i |\psi_{i_{\text{surf}}}(\boldsymbol{r})|^2. \tag{48}$$

In the context of STM, only states near the highest occupied and lowest unoccupied molecular orbitals (HOMO and LUMO) are relevant, given by the index set i_{surf}. Surface states may be identified using a layer-by-layer analysis of Mulliken charges. Another restriction on the index set is that subsets of degenerate states, recognizable by computationally equal eigenvalues, must be included in their entirety in order to fully represent the symmetry group of the wavefunction. To obtain images, the charge density is plotted logarithmically on a plane parallel to the surface or planar molecule, separated from the surface by about an ångström.

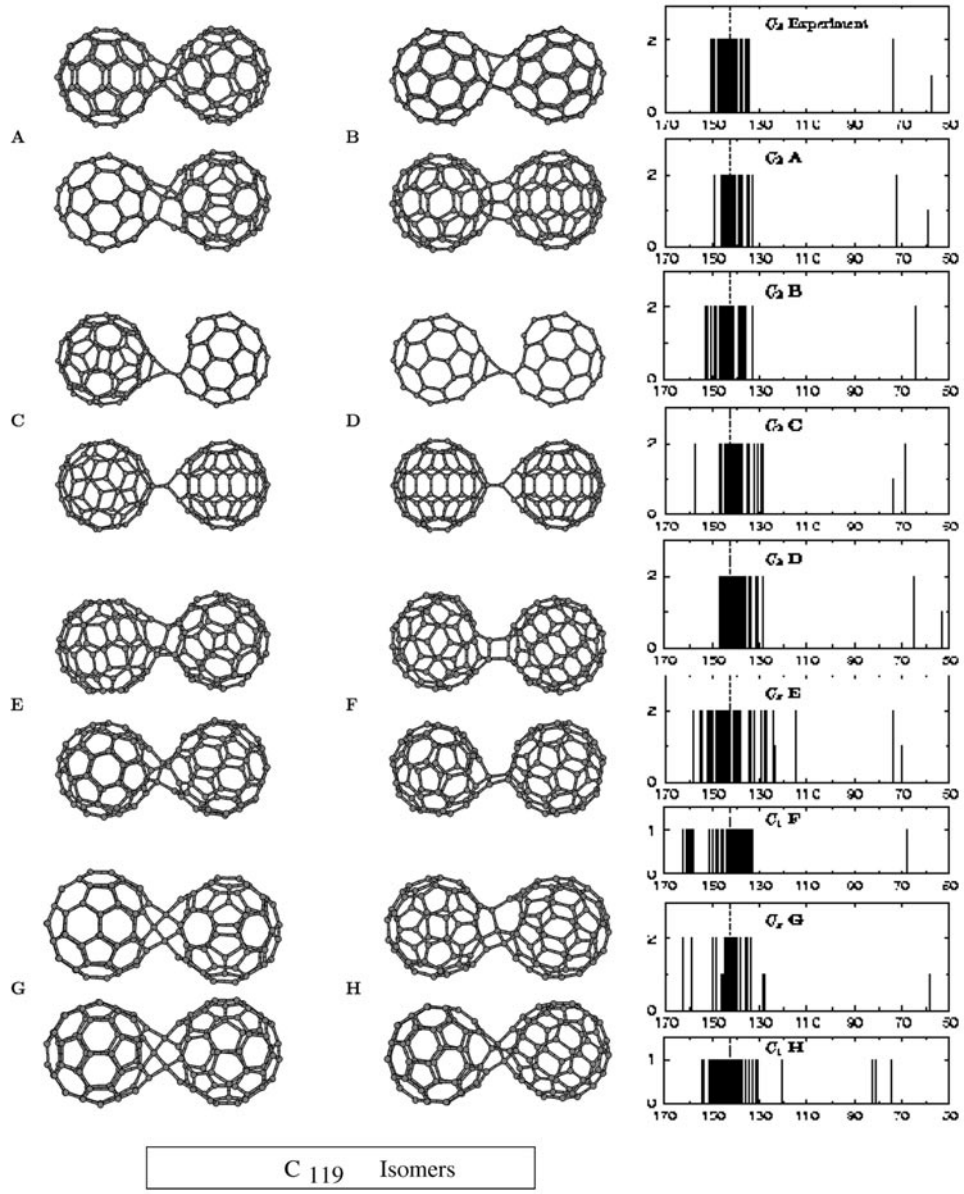

Figure 10. Optimized structures of eight isomers of C_{119} (A–H, left panel) and the ^{13}C NMR pattern of these isomers [104].

The formalism above was applied first to diamond surfaces [108, 109], where it became evident that surface charge densities from clean and hydrogenated diamond surfaces differ significantly due to the disappearance of true surface states upon hydrogen saturation; see figure 11. Another application was to small organic molecules [110, 111], deposited on conducting substrates such as graphite. In these situations, the HOMO and LUMO often show different morphologies, which help to identify the molecules.

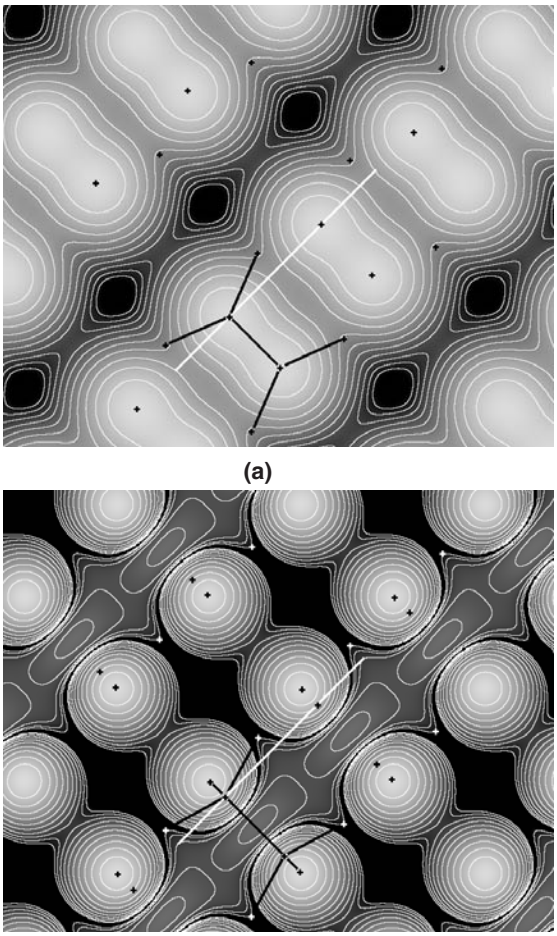

Figure 11. Surface charge density for the C(100)-(2×1) reconstruction indicating the influence of hydrogen termination. Height: 1.3 Å above topmost C atoms. Area: 10.6 Å × 8.5 Å. (*a*) Clean reconstruction, orbital one below HOMO. (*b*) Hydrogenated reconstruction, LUMO. The black lines indicate a dimer bonded to the first C subsurface layer. Positions of atoms in the layers closest to the cutting plane are marked. The white line indicates the position selected for vertical cuts; see [109].

4.7. Green function approach to transport properties

A recent area of interest is the study of the electronic properties of nanotechnological devices based on organic–inorganic materials. The description of the device properties requires exact boundary conditions. The Green function (GF) technique [112] allows an exact coupling between a molecule and semi-infinite leads. A schematic diagram of the device is shown in figure 12. It consists of a central molecule, designated M, and a number of contacts $\mu = \alpha, \beta, \ldots$. The retarded Green function $\mathbf{G}^R(E)$ of such a system is defined as

$$\mathbf{G}^R(E) = \lim_{\eta \to 0} (E\mathbf{S} - \mathbf{H} + \mathrm{i}\eta)^{-1}. \tag{49}$$

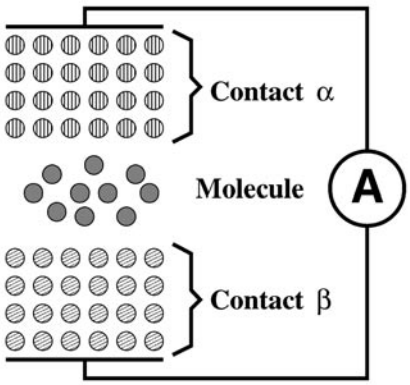

Figure 12. A schematic diagram of the device consisting of a molecule and two contacts, α and β.

Within a real-space basis, the Hamiltonian and overlap matrices separate into block-matrix form [113, 114]:

$$\mathbf{H} = \begin{pmatrix} \mathbf{H}_\alpha & \mathbf{T}_{\alpha M} & 0 \\ \mathbf{T}_{M\alpha} & \mathbf{H}_M & \mathbf{T}_{M\beta} \\ 0 & \mathbf{T}_{\beta M} & \mathbf{H}_\beta \end{pmatrix}$$
$$\mathbf{S} = \begin{pmatrix} \mathbf{S}_\alpha & \mathbf{S}_{\alpha M} & 0 \\ \mathbf{S}_{M\alpha} & \mathbf{S}_M & \mathbf{S}_{M\beta} \\ 0 & \mathbf{S}_{\beta M} & \mathbf{S}_\beta \end{pmatrix}. \tag{50}$$

The submatrices allow us to calculate separate GFs for the molecule and the contacts. For an isolated contact the GF reads

$$g_\mu(E) = \lim_{\eta \to 0} (E\mathbf{S}_\mu - \mathbf{H}_\mu + \mathrm{i}\eta)^{-1}. \tag{51}$$

The contact can be thought of as a semi-infinite repetition of so-called *principal layers* (PLs). A PL is a repetition unit which is thick enough that only nearest-neighbour PLs interact. From the intra-layer and inter-layer Hamiltonians and overlap matrix elements, the g_μ can be calculated exactly in a fast iteration scheme known as the *decimation technique* [115]. This technique takes into account all interactions between 2^n PLs in the nth iteration step.

The GF of the molecule, $\mathbf{G}_M$, is coupled to those of the contacts, g_μ by the self-energy operators $\Sigma_\mu(E)$, which are defined by the contact GF and the contact–molecule coupling submatrices $\mathbf{T}_{M\mu}$ and $\mathbf{S}_{M\mu}$:

$$\Sigma_\mu = (E\mathbf{S}_{M\mu} - \mathbf{T}_{M\mu}) g_\mu (E\mathbf{S}_{\mu M} - \mathbf{T}_{\mu M}). \tag{52}$$

With the self-energy operators, the GF of the molecule is

$$\mathbf{G}_M = (E\mathbf{S}_M - \mathbf{H}_M - \Sigma_\alpha - \Sigma_\beta)^{-1}. \tag{53}$$

Finally, the transmission coefficient can be calculated [116] as

$$T(E) = \mathrm{Tr}(\mathbf{\Gamma}_\alpha \mathbf{G}_M \mathbf{\Gamma}_\beta \mathbf{G}_M^\dagger), \tag{54}$$

where $\mathbf{\Gamma}_\mu$ are the spectral functions of the self-energy operators:

$$\mathbf{\Gamma}_\mu = \mathrm{i}(\Sigma_\mu - \Sigma_\mu^\dagger). \tag{55}$$

As an example for an application to transport properties within the new implementation we show the calculation of the current in a nanotube-based field-effect transistor (FET). The atomic

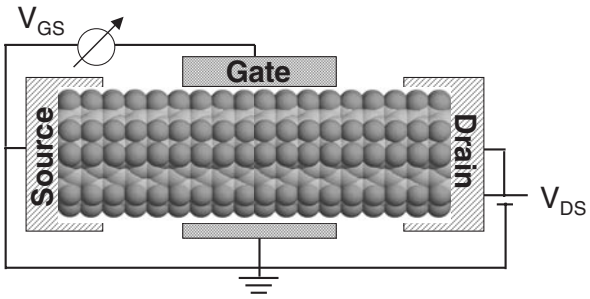

Figure 13. A schematic drawing of a fluorinated carbon nanotube-based field-effect transistor (FCN–FET).

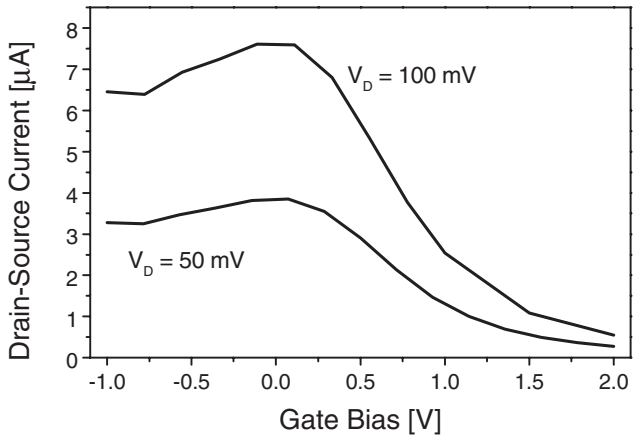

Figure 14. Calculated drain current as a function of the gate bias for two drain biases in the fluorinated carbon nanotube FET.

structure of the simulated device is shown in figure 13. We use a fluorinated nanotube [117] to connect the source and drain contacts. As in a conventional FET, the current is modulated by the gate electrode. Similar devices, with carbon nanotubes, have been investigated experimentally by several authors [118–121]. The calculated drain–source current as a function of the gate bias is shown in figure 14. For a given drain bias the device presents two distinct regions separated by zero bias voltage. For negative gate bias the current reaches a positive saturation value while for positive gate bias it approaches zero. At $V_{GS} = 2$ V the current is essentially negligible and we can consider the 'channel' of the FET as being pinched off. On reducing the drain bias the current also diminishes. Indeed, we observe an almost linear dependence of I_{DS} in the saturation region as a function of V_{DS}. We should point out that the results shown are in good agreement with those reported in [121]. Summarizing, we have shown that density-functional-based tight-binding methods can be efficiently coupled to Green function techniques in order to account for current flow in nanoscale structures.

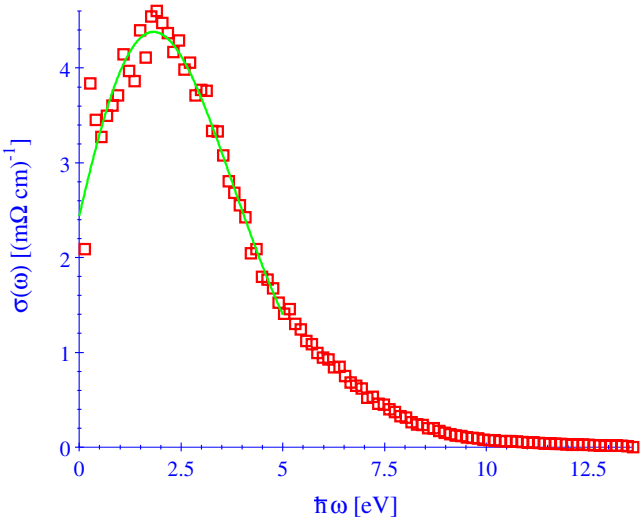

Figure 15. The calculated $\sigma(\omega)$ dependence for liquid Na_xSn_{1-x}, $x = 0.2$. (This figure is in colour only in the electronic version)

4.8. Conductivity

Within the Kubo–Greenwood (KG) theory [122] the electrical (AC) conductivity can be calculated as

$$\sigma(\omega) = \frac{2\pi e^2}{3m_e^2\omega\Omega} \sum_i^{\text{occ}} \sum_j^{\text{unocc}} \sum_\alpha |\langle\psi_i|\hat{p}_m|\psi_j\rangle|^2 \delta(\varepsilon_j - \varepsilon_i - \hbar\omega), \tag{56}$$

where m_e and e are the electronic mass and charge, respectively, Ω is the MD cell volume and $\hat{p}_m$ is the m-component of the momentum operator. The sum over i and j runs over occupied and unoccupied states, respectively—corresponding to the one-particle eigenvalues (from the Kohn–Sham equation) ε_i and ε_j as well as the one-particle wavefunctions ψ_i and ψ_j, respectively.

This formula may be compared with the 'joint density of states' with 'weight factors' $|\langle\psi_i|\hat{p}_m|\psi_j\rangle|^2$ for each contribution.

The combination of the KG formalism with MD allows the calculation of the electric conductivity in rather complex disordered systems—e.g. liquids—at finite temperatures. To obtain the conductivity from MD simulations, one has to average $\sigma(\omega)$ over the whole trajectory of a MD run—in a similar manner as for structure factors, for example [123]. By this procedure the effects of the ionic motion on the conductivity are implicitly considered. Finally, the extrapolation $\omega \to 0$ gives the DC conductivity.

We have implemented the KG formalism in our DFTB scheme and applied it as an example for the calculation of the concentration dependence in liquid Zintl alloys [123]. Within our DFTB scheme the calculations with the KG formula can be performed very quickly. Thus we were able to show that it is sufficient to take into account just a limited number of configurations. To obtain the DC conductivity, an extrapolation $\omega \to 0$ of $\sigma(\omega)$ had to be performed. As to illustration, the calculated $\sigma(\omega)$ dependence for liquid Na_xSn_{1-x}, $x = 0.2$, is shown in figure 15.

The calculated DC resistivities from the DFTB calculation for the liquid NaSn system as a function of the composition are summarized in table 2, in comparison to experimental as well

Table 2. Resistivities of NaSn alloys with different compositions, in $\mu\Omega$ cm.

% Na	Experiment [124]	*ab initio* calculation	DFTB calculation
20	110 ± 0.2	227 ± 50	230 ± 80
40	274 ± 1	312 ± 80	400 ± 100
50	426 ± 5	383 ± 80	800 ± 200
57	658 ± 10	869 ± 90	850 ± 200
80	426 ± 5	408 ± 100	180 ± 100

as *ab initio* data [10, 123]. As can be seen, the DFTB calculations agree qualitatively with the experimental and the *ab initio* data and they describe the concentration dependence correctly.

5. Summary

The present article summarizes the current status of development and application within the DFTB method. This approximate but still predictive scheme allows one to perform electronic structure calculations on large-scale systems which cannot be handled with *ab initio* or first-principles methods. Special emphasis was laid on the description of excited states. Here we adapt recent extensions of the standard DFT methodology to our scheme by taking advantage of the typical DFTB kind of approximation in order to increase numerical efficiency. Within the regime of linear response this opens up the possibility of calculating optical spectra of technologically relevant materials, while for high intensity of the external fields, information related to the active field of pump–probe spectroscopy may be obtained.

In addition, the DFTB approach may be used to calculate a variety of different material properties, which are directly accessible by experiment. On the one hand, it is therefore possible to validate the quality of the theoretical data and, on the other hand, theory may assist in the interpretation of experimental results or predict new phenomena. As an example, from section 4.1, comparison of theoretical and experimental IR intensities leads to a microscopic understanding of the chemical bonding situation in amorphous films, whereas in section 4.5 it was shown how calculated NMR patterns helped to identify the dominant isomer of the fullerene C_{119}.

Together with this strong link to experiment and our efforts to cope with larger and larger system sizes, we hope that the DFTB approach provides a method for tackling the new challenges in nanoscale materials science.

Acknowledgments

The authors acknowledge support from the Deutsche Forschungsgemeinschaft for various projects. Further, the EC-DIODE-Network has particularly contributed to extending our applications to organic thin films and device structures. Finally, many fruitful collaborations should be mentioned, which by addressing different applications have contributed to the success of our DFTB method.

References

[1] Stillinger F H and Weber T H 1985 *Phys. Rev.* B **31** 5262
[2] Tersoff J 1986 *Phys. Rev. Lett.* **56** 632
Tersoff J 1998 *Phys. Rev.* B **37** 6991
[3] Brenner D W 1990 *Phys. Rev.* B **42** 9458

[4] Brooks B R, Burccoleri R E, Olafson B D, States D J, Swaminathan S and Karplus M 1983 *J. Comput. Chem.* **4** 187
MacKerell A D *et al* 1998 *J. Phys. Chem.* B **102** 3586
[5] Cornell W D *et al* 1995 *J. Am. Chem. Soc.* **117** 5179
[6] Hehre W, Radom L, Schleyer P and Pople J 1986 *Ab-Initio Molecular Orbital Theory* (New York: Wiley)
[7] Foulkes W M C, Mitas L, Needs R J and Rajagopal G 2001 *Rev. Mod. Phys.* **73** 33
[8] Hohenberg P and Kohn W 1964 *Phys. Rev.* **136** B864
[9] Kohn W and Sham L J 1965 *Phys. Rev.* **140** A1133
[10] Car R and Parrinello M 1985 *Phys. Rev. Lett.* **55** 2471
[11] Bilek M M M, McKenzie D R, McCulloch D G and Goringe C M 2000 *Phys. Rev.* B **62** 3071
[12] Runge E and Gross E K U 1984 *Phys. Rev. Lett.* **52** 997
[13] de Shalit A and Feshbach H 1974 *Theoretical Nuclear Physics* vol 1 (New York: Wiley) p 530
[14] Goringe C M, Bowler D R and Hernandez E 1997 *Rep. Prog. Phys.* **60** 1447
[15] Turchi P E A, Gonis A and Colombo L (ed) 1998 *Tight-Binding Approach to Computational Materials Science* vol 491 (Pittsburgh, PA: Materials Research Society)
[16] Finnis M W, Paxton A T, Methfessel M and van Schilfgaarde M 1998 The crystal structure of zirconia from first principles and self consistent tight binding *Phys. Rev. Lett.* **81** 5149–52
[17] Fabris S, Paxton A T and Finnis M W 2002 Simulation of stabilised and partially stabilised zirconia with a self-consistent tight-binding model *J. Am. Ceram. Soc.* submitted
[18] Fabris S, Paxton A T and Finnis M W 2001 Free energy and molecular dynamics calculations for the cubic-tetragonal phase transition in zirconia *Phys. Rev.* B **63** published 26 January, 094101-1-13
[19] Lee X P, Nunes W and Vanderbilt D 1993 *Phys. Rev.* B **47** 10 891
[20] Kim J, Mauri F and Galli G 1995 *Phys. Rev.* B **52** 1640
[21] Yang W 1991 *Phys. Rev. Lett.* **66** 1438
Yang W and Lee T S 1995 *J. Chem. Phys.* **163** 5674
[22] Elstner M, Porezag D, Jungnickel G, Elsner J, Haugk M, Suhai S, Seifert G and Frauenheim T 1998 *Phys. Rev.* B **58** 7260
[23] Frauenheim T, Seifert G, Elstner M, Hajnal Z, Jungnickel G, Porezag D, Suhai S and Scholz R 2000 *Phys. Status Solidi* b **217** 41
[24] Seifert G, Eschrig H and Bieger W 1986 *Z. Phys. Chem.* **267** 529
[25] Porezag D, Frauenheim T, Köhler T, Seifert G and Kaschner R 1995 *Phys. Rev.* B **51** 12 947
[26] Haugk M, Elsner J, Frauenheim T, Seifert G and Sternberg M 2000 *Phys. Status Solidi* b **217** 473
[27] Elstner M, Frauenheim T, Kaxiras E, Seifert G and Suhai S 2000 *Phys. Status Solidi* b **217** 375
[28] Runge E and Gross E K U 1984 *Phys. Rev. Lett.* **52** 997
[29] Gross E K U and Kohn W 1990 *Adv. Quantum Chem.* **21** 255
[30] Peyerimhoff S D and Buenker R J 1978 *Excited States in Chemistry* ed C A Nikolaides and D R Beck (Dordrecht: Reidel)
[31] Roos B O, Fülscher M, Malmqvist P-A, Merchan M and Serrano-Andres L 1995 *Quantum Mechanical Electronic Structure Calculations with Chemical Accuracy* ed S R Langhoff (Dordrecht: Kluwer)
[32] Hedin L 1965 *Phys. Rev.* **139** A796
[33] Kootstra F, de Boeij P L and Snijders J G 2000 *Phys. Rev.* B **62** 7071
[34] Kootstra F, de Boeij P L and Snijders J G 2000 *J. Chem. Phys.* **112** 6517
[35] Vasiliev I, Öğüt S and Chelikowsky J R 1999 *Phys. Rev. Lett.* **82** 1919
[36] Vasiliev I, Öğüt S and Chelikowsky J R 1999 *Phys. Rev.* B **60** R8477
[37] Bauernschmitt R and Ahlrichs R 1996 *Chem. Phys. Lett.* **256** 454
[38] Fabian J 2001 *Theor. Chem. Acc.* **106** 199
[39] Casida M E 1995 *Recent Advances in Density Functional Methods* vol 1, ed D P Chong (Singapore: World Scientific) p 155
[40] Casida M E 1996 *Recent Developments and Applications of Modern Density Functional Theory* vol 4, ed J M Seminario (Amsterdam: Elsevier) p 391
[41] Niehaus T A, Suhai S, Della Sala F, Lugli P, Elstner M, Seifert G and Frauenheim T 2001 *Phys. Rev.* B **63** 085108
[42] Ridley J and Zerner M C 1973 *Theor. Chem. Acta* **32** 111
[43] Niehaus T A 2001 *PhD Thesis* Universität Paderborn
http://ubdata.uni-paderborn.de/ediss/06/2001/niehaus/index.htm
[44] Yabana K and Bertsch G F 1999 *J. Quantum Chem.* **75** 55
[45] Ullrich C A, Gossmann U J and Gross E K U 1999 *Ber. Bunsenges. Phys. Chem.* **99** 488
[46] Torralva B, Niehaus T A, Elstner M, Frauenheim T, Suhai S and Allen R E 2001 *Phys. Rev.* B **64** 153105

[47] Allen R E 1994 *Phys. Rev.* B **50** 18 629
[48] Graves J S and Allen R E 1998 *Phys. Rev.* B **58** 627
[49] Todorov T N 2001 *J. Phys.: Condens. Matter* **13** 10 125–48
[50] Saalmann U and Schmidt R 1996 *Z. Phys.* D **38** 153
[51] Graf M and Vogl P 1995 *Phys. Rev.* B **51** 4940
[52] Press W, Flannery B, Teukolsky S and Vetterling W 1988 *Numerical Recipes in FORTRAN* (Cambridge: Cambridge University Press)
[53] Eschrig H 1988 *Optimized LCAO Method and the Electronic Structure of Extended Systems* (Berlin: Springer)
[54] Eschrig H and Bergert I 1978 *Phys. Status Solidi* b **90** 621
[55] Janak J F 1978 *Phys. Rev.* B **18** 7165
[56] Blackford L S *et al* 1997 *Proc. Supercomputing ScaLAPACK User's Guide* (3600 University City Science Center) (Philadelpha, PA: SIAM)
[57] Aboelaze M, Chrisochoides N and Houstis E 1991 *Technical Report* CSD-TR-91-007 (Purdue University, West Lafayette, IN)
[58] Choi J, Dongarra J, Ostrouchov S, Petitet A, Walker D and Whaley R C 1995 *Computer Science Technical Report* CS-95-292 (University of Tennessee, Knoxville, TN)
[59] Choi J, Dongarra J and Walker D 1996 *Concurrency: Practice Experience* **8** 517
[60] Goedecker S 1999 *Rev. Mod. Phys.* **71** 1085
[61] Galli G 2000 *Phys. Status Solidi* b **217** 231
[62] Yang W and Perez-Jorda J M 1998 Linear scaling methods for electronic structure calculations *Encyclopedia of Computational Chemistry* ed P Schleyer (New York: Wiley)
[63] Stephan U 2000 *Phys. Rev.* B **62** 16 412
[64] Sternberg M, Galli G and Frauenheim T 1999 *Comput. Phys. Commun.* **118** 200
[65] Yang W 1991 *Phys. Rev. Lett.* **66** 1438
[66] Yang W and Lee T-S 1995 *J. Chem. Phys.* **163** 5674
[67] Liu H Y, Elstner M, Kaxiras E, Frauenheim T, Hermans J and Yang W T 2001 *Proteins* **44** 484
[68] Elstner M, Liu H Y, Kaxiras E, Frauenheim T, Hermans J and Yang W T 2002 in preparation
[69] Gao J 1996 Methods and applications of combined quantum mechanical and molecular mechanical potentials *Reviews in Computational Chemistry* vol 7, ed K B Lipkowitz and D B Boyd (New York: Academic) p 119
[70] Mordasini T Z and Thiel W 1998 *Chimia* **52** 288
[71] Elstner M 1998 *PhD Thesis* Universität Paderborn
[72] Han W G, Elstner M, Jalkanen K J, Frauenheim T and Suhai S 2000 *Int. J. Quantum Chem.* **78** 459
[73] Cui Q, Elstner M, Kaxiras E, Frauenheim T and Karplus M 2001 *J. Phys. Chem.* B **105** 569
[74] Snoke D W and Cardona M 1993 *Solid State Commun.* **87** 12
[75] Niehaus T, Elstner M, Frauenheim T and Suhai S 2001 *J. Mol. Struct. (Theochem)* **541** 185
[76] Porezag D, Jungnickel G, Frauenheim T, Seifert G, Ayuela A and Pederson M R 1997 *Appl. Phys.* A **64** 321
[77] Krause M, Dunsch L, Seifert G, Gromov A, Krätschmer W, Gutierrez R, Porezag D and Frauenheim T 1998 *J. Chem. Soc. Faraday Trans.* **94** 2287
[78] Krause M, Kuzmany H, Georgi P, Dunsch L, Vietze K and Seifert G 2002 *J. Chem. Phys.* at press
[79] Bohr H G, Jalkanen K J, Elstner M, Frimand K and Suhai S 1999 *Chem. Phys.* **246** 13
[80] Köhler T, Frauenheim T and Jungnickel G 1995 *Phys. Rev.* B **52** 11 837
[81] Frauenheim T, Köhler T, Sternberg M, Porezag D and Pederson M R 1996 *Thin Solid Films* **272** 314
[82] Lehmann G, Hess P, Wu J J, Wu C T, Wong T S, Chen K H, Chen L C, Lee H Y, Amkreutz M and Frauenheim T 2001 *Phys. Rev.* B **64** 165305
[83] Vietze K, Seifert G and Fowler P W 2000 *Proc. 14th Int. Winter School on Electronic Properties of Novel Materials* ed H Kuzmany, J Fink, M Mehring and S Roth (New York: AIP) p 131
[84] Heinze H H, Görling A and Rösch N 2000 *J. Chem. Phys.* **113** 2088
[85] Zeiger H J, Vidal J, Cheng T K, Ippen E P, Dresselhaus G and Dresselhaus M S 1991 *Phys. Rev.* B **45** 768
[86] Dexheimer S L, Mittleman D M, Schoenlein R W, Vareka W, Xiang X-D, Zettl A and Shank C V 1993 *Ultrafast Phenomena* vol 8, ed J L Martin, A Migus, G A Mourou and A H Zewail (Heidelberg: Springer)
[87] Eklund P C, Zhou P, Wang K-A, Dresselhaus G and Dresselhaus M S 1992 *J. Phys.: Condens. Matter* **53** 1391
[88] Dhar L, Rogers J and Nelson K A 1994 *Chem. Rev.* **94** 157
[89] Scholz M and Köhler H J 1981 *Quantenchemische Näherungsverfahren und Ihre Anwendung in der Organischen Chemie* (Berlin: VEB Deutscher Verlag der Wissenschaften)
[90] Pople J A, Beveridge D L and Dobosh P A 1968 *J. Am. Chem. Soc.* **90** 4201
[91] Köhler C, Seifert G, Gerstmann U, Elstner M, Overhof H and Frauenheim T 2001 *Phys. Chem. Chem. Phys.* **3** 5109
[92] *Landolt–Börnstein New Series* 1977 Group II, vol 9b, ed H Fischer and K H Hellwege (Heidelberg: Springer)

[93] *Landolt–Börnstein New Series* 1980 Group II, vol 9d1, ed H Fischer and K H Hellwege (Heidelberg: Springer)
[94] *Landolt–Börnstein New Series* 1987 Group II, vol 17c, ed H Fischer and O Madelung (Heidelberg: Springer)
[95] Frisch M J *et al* 1998 *Gaussian* (Revision A.7) (Gaussian Inc., Pittsburgh, PA)
[96] Gano J E, Jacob E J, Sekher P, Subramaniam G, Eriksson L A and Lenoir D 1996 *J. Org. Chem.* **61** 6739
[97] Rajagopal A K and Callaway J 1973 *Phys. Rev.* B **7** 1912
[98] Eschrig H, Seifert G and Ziesche P 1985 *Solid State Commun.* **56** 777
[99] Bieger W, Seifert G, Eschrig H and Großmann G 1985 *Chem. Phys. Lett.* **115** 275
[100] Friedrich K, Seifert G and Großmann G 1990 *Z. Phys.* D **17** 45
[101] Kutzelnigg W 1980 *Isr. J. Chem.* **19** 193
[102] Schindler M and Kutzelnigg W 1982 *J. Chem. Phys.* **76** 1919
[103] Gromov A, Ballenweg S, Lebedkin S, Hull W E and Krätschmer W 1997 *Chem. Phys. Lett.* **267** 460
[104] Heine T, Zerbetto F, Seifert G and Fowler P 2000 *J. Phys. Chem.* A **104** 3865
[105] Heine T, Seifert G, Fowler P and Zerbetto F 1999 *J. Phys. Chem.* A **103** 8738
[106] Binnig G and Rohrer H 1987 *Rev. Mod. Phys.* **59** 615
[107] Tersoff J and Hamann D R 1985 *Phys. Rev.* B **31** 805
[108] Köhler T, Sternberg M, Porezag D and Frauenheim T 1996 *Phys. Status Solidi* a **154** 69
[109] Sternberg M, Frauenheim T, Zimmermann-Edling W and Busmann H G 1997 *Surf. Sci.* **370** 232
[110] Walzer K, Sternberg M and Hietschold M 1998 *Surf. Sci.* **415** 376
[111] Scholz R, Kobitski A Y, Kampen T U, Schreiber M, Zahn D T R, Jungnickel G, Elstner M, Sternberg M and Frauenheim T 2000 *Phys. Rev.* B **61** 13 659
[112] Datta S 1995 *Electronic Transport in Mesoscopic Systems (Cambridge Studies in Semiconductor Physics and Microelectronic Engineering vol 3)* (Cambridge: Cambridge University Press) chs 3 and 8
[113] Mujica V, Kemp M and Ratner M A 1994 *J. Chem. Phys.* **101** 6894
[114] Mujica V, Kemp M and Ratner M A 1994 *J. Chem. Phys.* **101** 6856
[115] Guinea F, Tejedor C, Flores F and Louis E 1983 *Phys. Rev.* B **28** 4397
[116] Samanta M P, Tian W, Datta S, Henderson J I and Kubiak C P 1996 *Phys. Rev.* B **53** R7626
[117] Seifert G, Köhler T and Frauenheim T 2000 *Appl. Phys. Lett.* **77** 1313
[118] Tans S J, Devoret M H, Dai H, Thess A, Smalley R E, Georliga L J and Dekker C 1997 *Nature* **386** 474
[119] Bockrath M, Cobden D H, McEuen P L, Chopra N G, Zettl A, Thess A and Smalley R E 1997 *Science* **275** 1922
[120] Tans S J, Verschueren A R M and Dekker C 1998 *Nature* **396** 49
[121] Martel R, Schmidt T, Shea H R, Hertel T and Avouris P 1998 *Appl. Phys. Lett.* **73** 2447
[122] Economou E N 1983 *Green Functions in Quantum Physics* vol 7 (Heidelberg: Springer)
Economou E N 2000 *Phys. Rev.* B **61** 13 659
[123] Seifert G, Kaschner R, Schöne M and Pastore G 1998 *J. Phys.: Condens. Matter* **10** 1175
[124] van der Marel C, van Oosten A B, Geertsma W and van der Lugt W 1982 *J. Phys. F: Met. Phys.* **12** 2349